Degassing from magma reservoir to eruption in silicic systems

Julia Neukampf, Oscar Laurent, Peter Tollan, Anne-Sophie Bouvier, Tomas Magna, Peter Ulmer, Lydéric France, Ben Ellis, Olivier Bachmann

Degassing from magma reservoir to eruption in silicic systems: the Li elemental and isotopic record from rhyolitic melt inclusions and host quartz in a Yellowstone rhyolite

Julia Neukampf[1,2], Oscar Laurent[1,3], Peter Tollan[1], Anne-Sophie Bouvier[4], Tomas Magna[5], Peter Ulmer[1], Lydéric France[2], Ben S. Ellis[1] and Olivier Bachmann[1]

[1]*Institute of Geochemistry and Petrology, ETH Zurich, NW Clausiusstrasse 25, CH-8092, Zurich, Switzerland*

[2]*Université de Lorraine, CNRS, CRPG, F-54000 Nancy, France*

[3]*CNRS, Géosciences Environnement Toulouse, Observatoire Midi-Pyrénées, 14 avenue Édouard Belin F-31400 Toulouse, France*

[4]*Institut des Sciences de la Terre, University of Lausanne, CH-1015, Lausanne, Switzerland*

[5]*Czech Geological Survey, Klárov 3, CZ-11821 Prague 1, Czech Republic*

*Corresponding author: Email: julia.neukampf@univ-lorraine.fr

For submission to GEOCHIMICA ET COSMOCHIMICA ACTA

Abstract

Lithium and hydrogen are volatile elements which diffuse rapidly in crystals and melt, making them powerful geochemical tools to reconstruct geological processes that take place on short time scales, such as syn- and post-eruptive degassing. Although the dynamics of hydrogen are fairly well understood to better constrain such processes, the assessment of Li behaviour within the magma reservoir relevant for ascent-related degassing still lacks detailed evaluation. Here, the first *in situ* Li concentrations and isotopic compositions (using SIMS analysis) of rhyolitic quartz-hosted, naturally glassy or crystallised melt inclusions (MIs) and groundmass glass (Mesa Falls Tuff, Yellowstone) are used to reconstruct Li elemental and isotopic evolution in the magma reservoir. Lithium concentrations in quartz-hosted glassy MIs (10–61 ppm) from a fallout deposit overlap with their groundmass glass (32–46 ppm) and their host quartz (8–15 ppm). Crystallised MIs from a later erupted flow pumice clast sample have higher Li concentrations (8–190 ppm) compared to the groundmass glass (32–51 ppm) and their host-quartz (15–24 ppm). Li content in quartz from the early erupted sample is relatively homogenous, whereas it is up to a factor of two higher in the later erupted sample and heterogeneous, with a simultaneous increase in Li versus a decrease in H towards crystal rims. The δ^7Li difference (expressed as $\Delta^7Li_{MI-glass}$) between MIs (−8.0‰ to +12.3‰) and groundmass glass (+9.0‰ to +20.5‰) of two pyroclastic deposits reaches up to 29‰. Glassy MIs are internally heterogeneous in δ^7Li and Li abundance. The cores of the glassy MIs record the δ^7Li of the least modified melt during entrapment and the data distribution can be modelled by equilibrium fractionation between the melt and vapour phase during early open-system degassing in the magma reservoir. Late degassing during eruption triggers Li–H diffusional exchange between quartz and melt, as the degassing of H_2O and the accompanying pressure change trigger H diffusion out of the host quartz and the MIs, which is charge balanced

by Li inward diffusion. This results in the modification of Li contents in quartz and δ^7Li values in the rims of the glassy MIs. Crystallised MIs reflect the loss of H_2O from the MIs and the resulting enrichment of Li during the crystallisation. Additionally, the variations of δ^7Li in the groundmass glass can be explained through modelling by kinetic fractionation between the melt and vapour during late stage open-system degassing linked with magma ascent.

Keywords: Lithium isotopes, melt inclusions, open system degassing, diffusion, quartz, H_2O

Highlights:

- Glassy melt inclusions partially re-equilibrated with host-quartz upon degassing
- Modification of Li concentration in quartz by H–Li exchange
- Kinetic fractionation between the melt and vapour during late stage open-system degassing
- Equilibrium fractionation leading to large span in δ^7Li composition between different melt inclusions during early open-system degassing in magma reservoir

1. Introduction

In the last two decades an increasing number of studies have focused on the behaviour of lithium (Li) in different geochemical reservoirs. This has been driven chiefly by the unique chemical properties of Li, such as its typically rapid rates of diffusion in melts and crystals, its variably volatile behaviour and the large relative mass difference (17%) between ^{6}Li and ^{7}Li (e.g., Richter et al., 2003; Tomascak et al., 2016; Ellis et al., 2018; Beinlich et al., 2020; Neukampf et al., 2021). Challenges associated with the analysis of Li and its isotopes are now largely overcome through advances in modern mass spectrometry techniques (e.g., Chan and Edmond, 1988; Tomascak et al., 1999a; Kasemann et al., 2005). In igneous systems, most studies have focused on Li as a proxy to understand processes of crust–mantle recycling and seawater–oceanic crust interaction (e.g., Chan et al., 1992; Moriguti and Nakamura, 1998; Elliott et al., 2006; Magna et al., 2006; Tomascak et al., 2008). In contrast, the behaviour of Li in more evolved, silicic magmas at mid to upper crustal levels is poorly understood. Rhyolitic deposits are an important component of continental volcanic systems and play an important role in the element cycles (e.g., Ellis et al., 2013). Despite the fact that continental crust represents an important repository for Li (Teng et al., 2004), including all known economic deposits (e.g., Hofstra et al., 2013; Benson et al., 2017), studies focusing on Li elemental and isotopic compositions of pre-eruptive felsic systems are comparatively infrequent (e.g., Vlastélic et al., 2011; Charlier et al., 2012; Giuffrida et al., 2018; Holycross et al., 2018). Moreover, previous studies largely focused on magmatic systems along arcs (e.g., Gurenko et al., 2005; Bouvier et al., 2008, 2010; Schiavi et al., 2010, 2012) whereas other settings are less understood.

Available studies have shown that the Li concentration and isotopic composition of groundmass glass and mineral phases in silicic magmatic systems can be modified by syn- (e.g., Berlo et al.,

2004; Charlier et al., 2012; Neukampf et al., 2019; Neukampf et al., 2021; Viccaro et al., 2021) and post-eruptive processes (e.g., Ellis et al., 2018; Ellis et al., 2021), and thus may not represent the intrinsic pre-eruptive Li systematics, as theoretically considered by Watson (2017). The large relative mass difference between the two Li isotopes governs isotopic fractionation and leads to $^{7}Li/^{6}Li$ variations in nature (e.g., Tomascak et al., 2016). Although large $\delta^{7}Li$ variations on order of ~80‰ exist among distinct reservoirs such as seawater, carbonates, granites and mantle-derived rocks, $\delta^{7}Li$ variability in natural igneous rocks is probably not only source-driven. High-temperature diffusive fractionation between co-existing mineral phases (e.g., olivine, clino- and orthopyroxene) and melt at magmatic temperatures (above 800°C) has been recognised as an important process resulting in the Li isotopic disequilibrium in mafic igneous systems (e.g., Jeffcoate et al., 2007, Magna et al., 2008). Moreover, Richter et al. (2009) and Holycross et al. (2018) conducted experiments at magmatic temperatures which demonstrated that ^{6}Li diffuses ~3 to 3.5 % faster than ^{7}Li in dry and wet rhyolitic melt, respectively. The high and variable diffusivity of Li isotopes can cause large variations of Li concentration along chemical potential gradients and result in up to 40‰ kinetic fractionation of $^{7}Li/^{6}Li$ (Richter et al., 2003). The $\delta^{7}Li$ variations of this range can be observed within individual mineral phases at all scales, from a few microns (e.g., Jeffcoate et al., 2007; Parkinson et al., 2007; Lynn et al., 2018; Cisneros de León and Schmitt, 2019; Steinmann et al., 2020) up to several tens of meters (e.g., Lundstrom et al., 2005; Marschall et al., 2007; John et al., 2012; Beinlich et al., 2020). To provide further complexity to kinetic Li isotope behaviour, a recent study by Neukampf et al. (2021) on a flow pumice sample from the Mesa Falls Tuff (MFT; Fig. 1), Yellowstone, USA, showed that diffusive (kinetic) fractionation can lead to Li isotopic differences of >10‰ within single, otherwise chemically unzoned, plagioclase crystals.

In this context, retrieving the primary, pre-eruptive Li isotopic signature of magmas is particularly challenging. Melt inclusions (MIs) in phenocrysts are promising targets for this purpose, because they are considered to preserve the pre-eruptive melt composition upon entrapment (e.g., Roedder, 1979). However, MIs can be modified prior to eruption (e.g., Nielsen et al., 1998; Frezzotti, 2001; Rose-Koga et al., 2021). This can lead to compositional changes due to diffusive exchange between inclusions and host minerals and/or between host minerals and a surrounding melt (e.g., Qin et al., 1992; Danyushevsky et al., 2000). Diffusion between a host mineral and melt inclusion is deemed negligible once the sample has reached the fragmentation level in the conduit (e.g., Humphreys et al., 2008; Myers et al., 2016). Prior to eruption at rhyolitic temperatures (~800°C), changes in external conditions (particularly the pressure and, associatively, H_2O fugacity) result in chemical potential gradients that induce H diffusion out of MIs, leading to a loss of up to 80% of their original H_2O concentration within days (Severs et al., 2007; Myers et al., 2016; Myers et al., 2018; Myers et al., 2019). Because Li^+ has a similar charge, size and diffusivity to H^+, its composition in MIs can be modified in a similar way. Zajacz et al. (2009) experimentally determined that H_2O and Li contents in MIs can be modified at P–T conditions hypothesised for upper crustal silicic magma reservoirs. So far, this has not been investigated for natural rhyolitic samples even though Li could be used to determine decompression rates in a way similar to H_2O (e.g., Myers et al., 2016).

Quartz phenocrysts from a basal pumice from the MFT contains MIs that experienced only minor modification of their original volatile contents (Tollan et al., 2019), compared to MIs from other Yellowstone eruptions such as the Huckleberry Ridge Tuff (see below) (Myers et al., 2016). The MIs from the MFT are therefore ideal to investigate the behaviour of Li during pre- to syn-eruptive processes in silicic systems. The H_2O and CO_2 concentrations of MIs from the MFT are consistent

with the entrapment pressures of ~75–100 MPa (Tollan et al., 2019), indicating a very shallow upper crustal magma storage region before the final ascent. In this study, we report Li concentrations and isotopic compositions of quartz-hosted MIs and associated groundmass glass, complemented by Li concentrations of the host quartz from the MFT samples, previously characterised for H_2O and/or Li elemental/isotope systematics in quartz, quartz-hosted MIs, plagioclase, sanidine, fayalite, clinopyroxene, orthopyroxene, and groundmass glass (Tollan et al., 2019; Neukampf et al., 2019; Neukampf et al., 2021). This is the first data set from a rhyolitic eruptive unit which includes combined δ^7Li values, Li concentrations and H_2O concentrations of quartz-hosted MIs. The new data collected in this study are used to test the extent to which diffusion can modify the Li elemental and isotopic composition of MIs, and discuss the implications of Li mobility in terms of degassing processes.

2. Geological setting and samples

The Yellowstone caldera system is located at the northern end of the Snake River Plain hotspot track. It had three caldera-forming eruptions, the oldest and most voluminous Huckleberry Ridge Tuff (HRT; ~2500 km^3, 2.08 Ma; Christiansen, 2001; Rivera et al., 2014; Singer et al., 2014), the Mesa Falls Tuff (MFT; 280 km^3, 1.30 Ma; Christiansen, 2001; Rivera et al., 2016), and the Lava Creek Tuff (LCT; ~1000 km^3, 0.63 Ma; Christiansen, 2001; Matthews et al., 2015). The HRT and LCT erupted in multiple pulses, whilst the MFT erupted in a single pulse (Christiansen, 2001) and formed the Henry's Fork Caldera (Fig. 1). Its eruption was a voluminous explosive event with rapidly quenched fallout and pumice deposits at its base that were covered with a welded ignimbrite sheet (Rivera et al., 2016). This deposit is a high-silica rhyolite containing quartz, plagioclase, sanidine, fayalite, clinopyroxene, orthopyroxene, and accessory phases and

shows no significant chemical differences throughout the unit (Christiansen, 2001; Neukampf et al., 2019).

----INSERT FIGURE 1 Location Map----

Samples used in this study come from one sampling location (Fig. 1) and were collected from a thick ash and pumice pyroclastic density current deposited at the base of MFT. The basal pumice sample consists of cm-sized pumice and loose grains originating from highly vesicular MFT ash and pumice deposit at the base of MFT representing the onset of the eruption. This sample was previously analysed by Tollan et al. (2019) to determine H_2O and CO_2 concentrations of the glassy quartz-hosted MIs. We further characterised the sample in detail for major and trace element contents, and δ^7Li values. The flow pumice sample was collected from a stratigraphically different horizon that represents a later stage of the eruption. This latter sample is a large piece of a highly vesicular pumice clast sampled from an ash-flow sheet, deposited approximately two meters above the ash and pumice deposit. This flow pumice sample has been previously studied in detail by Neukampf et al. (2019) and Neukampf et al. (2021), who determined the major and trace element contents and δ^7Li values of all mineral phases present in the flow pumice sample. Considering the chemical and mineralogical homogeneity of the MFT and its interpretation as a single eruptive unit (Christiansen, 2001), both samples likely probe the same magma reservoir. These two samples were chosen to investigate the evolution of the melt and potential changes in the chemistry of the melt as a consequence of degassing during an explosive eruption so that the onset of the eruption can be compared with a later stage of the eruption. The choice of sampling from the non-welded

part of the MFT deposit was made to avoid overwhelming effects of post-eruptive processes that may further modify Li and H_2O concentrations (Lloyd et al., 2013; Ellis et al., 2018).

3. Materials and methods

3.1. Melt inclusion description

Quartz crystals from both samples from MFT are subhedral and range from 1 to 5 mm in diameter. The MIs occur as either naturally glassy or partly to fully crystallised. The glassy MIs types (Fig. 2 A–C), previously described by Tollan et al. (2019), range from transparent brown to colourless or bubble-bearing, with either spherical or negative crystal shapes, and a diameter between 10 and 450 µm. The crystallised MIs show a thin film (a few µm) of small quartz needles (approx. 5 to 15 µm) along the inclusion rims, and feldspar and quartz crystallised towards the inclusion interior (Fig. 2 D–F). Quartz grains from the basal pumice sample contain mostly glassy MIs with a subordinate proportion of crystallised MIs. Quartz grains from the flow pumice sample contain completely crystallised or opaque (partly crystallised) MIs, with only a minor population of glassy MIs. Forty-three glassy and 15 crystallised quartz-hosted MIs were selected for further geochemical investigation. We emphasise that the crystallised MIs were not re-homogenised as laboratory-controlled reheating of the MIs can lead to modifications of their volatile budget (e.g., Nielsen et al., 1998; Zajacz et al., 2009; Gaetani et al., 2012).

----INSERT FIGURE 2 Representative transmitted light images of double-polished quartz crystals and their melt inclusion populations. ----

3.2. Fourier transform infrared (FTIR) spectroscopy

Quartz crystals with MIs were hand-picked under a binocular microscope from crushed samples and mounted in 1-inch epoxy mounts. The quartz mounts were then double polished to a thickness of ~350 to ~450 µm. The H_2O and CO_2 contents of 12 crystallised quartz-hosted MIs were determined following the technique described in Tollan et al. (2019) where the H_2O and CO_2 contents of glassy quartz-hosted MIs can be found. In short, this method involves measuring MIs that remain fully enclosed in the crystal and then correcting for the absorbance contribution from the crystal host. First, transmitted light images of quartz crystals and their MIs were taken at the University of Bern using an optical microscope, recording their position, appearance and geometry (Fig. 2). The thickness of each quartz crystal was then measured using a Mitutoyo ID-S IP42 digital depth gauge (3 µm precision). FTIR spectra were obtained at the University of Bern with a Bruker Hyperion 3000 microscope attached to a Bruker Tensor II spectrometer. The measurements were conducted in a dry air-purged measurement chamber, using non-polarised light, 15× magnification using a Cassegrain objective and a HgCdTe detector. The light source and beamsplitter were composed of SiC and KBr, respectively. Background and sample measurements were made with 64 scans and a resolution of 8 cm^{-1}. Three measurements with a varying spot size were made on each melt inclusion, followed by the measurement immediately adjacent through the host quartz (without any inclusions in the beam pathway). The host quartz exhibited limited to absent interference absorption at the wavelengths of total H_2O and CO_2 in rhyolitic glass. Therefore, this latter step is solely used to obtain the Si–O overtone bands of the quartz for the calculation of the size of the melt inclusion, critical in the calculation of volatile abundance. The concentrations of H_2O and CO_2 were calculated using the (non-integrated) absorbance of the bands centred at 5200 cm^{-1}, 4500 cm^{-1} and 2345 cm^{-1}, with a direct baseline correction in each case. Conversion from the absorption to concentration was achieved using methods of Zhang et al. (1997) and Behrens et

al. (2004) for H_2O and CO_2, respectively. Three individual measurements on each melt inclusion were monitored for the consistency and any significant deviation in concentration resulted in discarding of the data. As noted by Tollan et al. (2019), any melt inclusion whose size was less than 15% of the thickness of the host quartz typically did not yield reliable values of concentration and was avoided from the H_2O and CO_2 calculations.

The H_2O content of the quartz crystals from the flow pumice sample was calculated based on the average core and rim measurements from 17 crystals. For each crystal, the OH bands in the wavenumber region 3600–3000 cm^{-1} were integrated, normalised to 1 cm and converted to H_2O using the integrated absorption coefficient of Thomas et al. (2009). Since the measurements consisted of non-polarised light and non-oriented crystals, the total absorbance was multiplied by a factor of 3 (Jackson et al. 2018). In addition to the melt inclusion measurements, high-resolution FTIR imaging and profiles of several quartz crystals were conducted to investigate the distribution of H throughout the quartz lattice. These FTIR images and profiles were obtained using a focal plane array (FPA) detector coupled to the FTIR setup described above. The measurements were conducted at a resolution of 8 cm^{-1} using a total of 128 scans. Pixels were binned three times, resulting in a spatial resolution of approximately 22×22 µm.

3.3. Secondary Ionization Mass Spectrometry (SIMS) measurements

Following the FTIR measurements, selected single MIs were exposed, polished and the quartz crystals hosting the MIs were excavated from the epoxy mount and mounted into a 1-inch indium mount for measurements of Li isotope compositions. Additionally, groundmass glass was hand-picked under a binocular microscope from crushed samples and mounted in 1-inch epoxy mounts for the measurements. Prior to the measurements backscattered electron (BSE) and

239 cathodoluminiscence (CL) images of the MIs, host quartz and groundmass glass were acquired
240 using a JEOL JSM-6390 LA scanning electron microscope (SEM), housed at the Institute of
241 Geochemistry and Petrology, ETH Zürich. The BSE images of groundmass glass and quartz
242 crystals were acquired with 15 kV acceleration voltage and CL images used 20 kV acceleration
243 voltage. Additionally, the quartz grains from the basal pumice sample with glassy MIs studied by
244 Tollan et al. (2019) for the contents of H_2O and CO_2, were included in the following geochemical
245 analysis.

246 Lithium isotope compositions were determined using a CAMECA ims1280-HR secondary
247 ionization mass spectrometer, housed at the SwissSIMS laboratory (University of Lausanne).
248 Samples were mounted in indium together with a reference material (either NIST SRM 612 or
249 BHVO-2G; Jochum et al., 2011). Prior to the analysis samples were coated with a 35 nm thick
250 gold layer. Sample surfaces were bombarded using an O^- beam generated by a Hyperion RF
251 source. The analyses were performed in three separate SIMS sessions; the intensity of the primary
252 O^- ion beam was ~2 nA in the first session whereas it was ~5 nA in the second and third session.
253 The $^6Li^+$ and $^7Li^+$ ion beams were collected in multi-collection mode using two opposing electron
254 multipliers. The mass resolution was set to 2400, using an entrance slit width of 121 μm and multi-
255 collector slits 1. The field aperture was closed to 1360, in order to avoid possible surface
256 contamination. Prior to each analysis, the surface was pre-sputtered for 200 s using a 15-μm raster
257 to remove the gold layer and any potential Li surface contamination. Automatic centring of the
258 field aperture and contrast aperture deflectors were conducted at the end of the pre-sputtering.
259 Measurements were performed using a 5-μm rastered primary beam. Each Li measurement
260 consisted of 70 cycles, with each cycle 12 s long. One to four measurements per inclusion were

performed depending on the inclusion size. In this study 43 glassy MIs in 21 quartz crystals and 15 crystallised MIs in 14 quartz crystals were analysed.

Calibration was made using StH, ATHO and Tl MPI-DING reference glass materials (Jochum et al., 2006). NIST SRM 612 and BHVO-2G were used to monitor the instrumental stability during the analytical sessions. Analyses of MIs were bracketed every four to five analyses by either NIST SRM 612 or BHVO-2G.

The measured data were corrected for an instrumental drift for each analytical session (typically 2–3‰ over an eight-hour period) using the Li isotopic composition of NIST SRM 612 or BHVO-2G measured throughout each session (Supplementary data – Table S13). The long-term reproducibility of the reference materials (2SD) after a drift correction is ±1.6‰ for NIST SRM 612 and ±2.3‰ for BHVO-2G. The internal error for each measurement is dependent on the Li content; it varied between ±0.3 and ±1.5‰ (2SE) during the course of this study. Lithium isotopic compositions are reported relative to the L-SVEC reference material (Flesch et al., 1973) and calculated as $\delta^7Li\ (‰) = [(^7Li/^6Li)_{sample}/(^7Li/^6Li)_{L-SVEC} - 1] \times 1000$.

3.4. Electron microprobe analyses (EPMA) measurements

Major and trace element contents of the MIs were measured following the SIMS analyses to minimise potential modifications of their Li isotopic composition. The major element compositions (Si, Na, Mg, Al, Ca, K, Ti, Fe, P, Cl, Cr, Mn, F) of the exposed MIs and the groundmass glass were determined with a Jeol JXA-8230 electron microprobe, housed at the Institute of Geochemistry and Petrology, ETH Zürich. All analyses were measured with 15 kV acceleration voltage. The beam diameter was either 2 µm with a beam current of 2 nA, 5 µm with a beam current of 4 nA, or 20 µm with a beam current of 10 nA, depending on the size of the MIs.

The beam diameter for the groundmass glass was 5 μm with a beam current of 4 nA. For Na, Si, Al, Mg, Ca and P, a counting time of 30 s on peak was used whereas a counting time of 20 s on peak was employed for K, Ti, Cl, Fe, Mn and Cr. Two to five individual measurements per melt inclusion were obtained. To ensure the reliability of the technique, the rhyolitic reference material VG-568 from the Smithsonian Institution (Supplementary TableS 9) was used as a secondary standard with the reproducibility better than 5% (SD).

3.5. Laser ablation inductively coupled plasma mass spectrometry (LA-ICP-MS)

Trace element concentrations in host quartz and quartz-hosted MIs were determined using the ETH prototype of the GeoLas laser ablation system equipped with a Compex Pro 102F (Coherent) Excimer 193 nm (ArF) laser source and coupled to a Nexion2000 (Perkin Elmer) fast-scanning quadrupole ICP-MS, housed at the Institute of Geochemistry and Petrology, ETH Zürich. The on-sample energy density of the laser beam was set to 20 $J \cdot cm^{-2}$ and the repetition rate was 10 Hz. Quartz crystals were measured with a spot size of 40 μm; for the glassy MIs the spot size was 10 to 40 μm, and one to seven measurements per inclusion were performed depending on the inclusion size. For crystallised MIs, one to nine measurements with a spot size of 40 μm was performed to account for the inherent compositional heterogeneity in the MI. The ablation was performed in an in-house cell designed for 1-inch mounts, using ca. 1.0 $l.min^{-1}$ He as carrier gas flow and ca. 1.0 $l.min^{-1}$ Ar make-up gas admixed downstream of the ablation chamber. All concentrations were quantified against the NIST SRM 610 glass wafer as the primary reference material (Jochum et al., 2011). The raw data were reduced using the Matlab-based SILLS program (Guillong et al., 2008) by using Si as internal standard for quartz (stoichiometric value), glassy MIs (as determined by EMPA) and crystallised MIs (average Si of glassy MIs). A natural quartz

crystal characterised by Audétat et al. (2015) was employed as a secondary reference material for quartz analyses (see Supplementary Table S8). The average 2 SD reproducibility of concentrations in the secondary quartz reference material for all analytical sessions was used to determine the uncertainties on the concentrations of unknown samples (5% relative for Li). For other element contents, the reproducibility on glassy MIs concentrations were on average 5% relative (2 SD) and for crystallised MIs 20% relative (2 SD).

In this study, we observed an offset of 20–50% in Li concentrations for LA-ICP-MS versus SIMS in the analysed MIs. In the following, we only use the Li concentrations determined by LA-ICP-MS for the interpretations, because the Li concentrations estimated by SIMS are less accurate. This is due to using ^{7}Li and primary intensity as a proxy for the yield and the relationship between yield and Li concentration can be non-linear depending on the matrix of the unknown sample (Hoover et al., 2021). When only the Li concentrations estimated by SIMS was available for our MIs, we have corrected the data using this above given offset.

4. Results

4.1. Major and trace element composition in melt inclusions

The MFT glassy MIs from the basal pumice sample have a chemical composition of a high-silica rhyolite (> 75 wt.% SiO_2, recalculated to a volatile-free basis) with Al_2O_3, K_2O and Na_2O ranging 11.5–12.6 wt.%, 5.2–5.9 wt.% and 1.6–3.5 wt.%, respectively (Supplementary Table S1). Furthermore, they are similar in their trace element composition compared to data for groundmass glass from the same sample (Neukampf et al., 2019) and similar MFT samples (Pearce et al., 1996; Perkins and Nash, 2002). However, the glassy MIs show a variability in trace element concentrations between different crystals (Table 1). Notably, Li shows larger relative variations

than most other elements in the population of glassy MIs, with Li concentrations from 10 to 61 ppm (basal pumice sample, average: 34 ppm; n = 104; n includes multiple analyses on single inclusions). Furthermore, seven out of the forty-three measured inclusions show a zonation in Li concentration (Fig. 3B) with up to 4 ppm higher Li concentration in their rims. The other MIs for which core-to-rim data was acquired were homogenous in their Li concentrations. There is no correlation between Li concentrations and the MI size, MI type or position in the quartz crystal.

----INSERT FIGURE 3 and TABLE 1 Lithium concentration in groundmass glass and melt inclusions. ----

Crystallised MIs from the flow pumice sample show a wider range in their trace element compositions compared to the glassy MIs from the basal pumice sample. They have higher Li concentrations (8–190 ppm; average 74 ppm; n = 44), overlapping those of the previously studied crystallised MIs from the same flow pumice sample from MFT (70–397 ppm, average: 244 ppm; n = 29; Neukampf et al., 2019). The differences between the Li concentrations measured in this study compared to the results of Neukampf et al. (2019) may be related to differences in the analytical method (exposed MIs, this study, versus unexposed MI bulk measurement, Neukampf et al., 2019). In contrast, the concentrations of other trace elements match well those of the glassy MIs (Table 1). Similar to the glassy MIs, there is no relationship between MI size and Li concentration. Only a few MIs show an increase of Li concentration towards their rims.

4.2. Trace element composition of quartz

The CL images of the quartz crystals from the two investigated samples show growth zones with no coherent patterns of internal zoning across the quartz populations (Fig. 4A–B; Supplementary Table S1 and S3). In quartz crystals from the flow pumice sample (Fig. 4A, 4C, 4E), P concentrations (8.8–19.2 ppm) are relatively homogeneous whereas Al (93–147 ppm) and Ti (60–151 ppm) show more substantial variations. Lithium concentrations in the flow pumice sample increase from the cores (15–24 ppm; n = 106) towards the rims (22–24 ppm; n = 7). All measured element patterns are in good agreement with the previously published values (Neukampf et al., 2019).

Quartz crystals from the basal pumice sample are compositionally similar to quartz from the flow pumice sample in most trace elements (e.g., Al = 88–117 ppm, Ti = 63–126 ppm) (Fig. 4.B, 4D, 4F), except Li. They indeed show more homogenous Li concentration from rims to cores compared to the flow pumice sample, but, at the same time, shifted to lower Li concentrations (8–15 ppm, average: 10 ppm; n = 184) by a factor of two. Thirteen trace element profiles were measured within five crystals from the basal pumice sample. Of the measured profiles six show an increase in Li concentration (10–30% relative) towards the MIs (Supplementary Table S3). Additionally, four trace element profiles indicate an increase of up to 3 ppm in Li abundance towards the crystal rims (Supplementary Table S3).

----INSERT FIGURE 4 Host quartz ----

4.3. Major and trace element composition in groundmass glass

The major element chemistry of the groundmass glass from the flow pumice sample resembles that of the composition of a high-silica rhyolite (> 75 wt.% SiO_2, recalculated to a

volatile-free basis) with Al_2O_3, Na_2O and K_2O ranging 11.7–12.9 wt.%, 2.1–3.3 wt.% and 5.3–6.3 wt.% (n= 94), respectively. All measured element contents are in good agreement with the previously published values from the same sample (Neukampf et al., 2019).

The groundmass glass from the basal pumice sample has a similar high-silica rhyolitic major element composition with Al_2O_3 ranging from 12.2 to 12.5 wt.%, Na_2O from 3.0 to 3.3 wt.% and K_2O from 5.5 to 5.7 wt.% (n= 23). The trace element abundances of groundmass glass in the two investigated samples are overlapping (Table 1). Lithium concentrations in groundmass glass from both samples are also overlapping, ranging from 32 to 51 ppm in the flow pumice sample (average 41 ppm; n = 66) and from 32 to 46 ppm in the basal pumice sample (average 41; n = 88; Fig. 3A).

4.4. H_2O and CO_2 in melt inclusions and host quartz

The calculated H_2O and CO_2 concentrations in crystallised MIs range from 2.2–3.8 wt.% and 120–470 ppm, respectively (Supplementary Table S1). The content of dissolved H_2O and CO_2 in the glassy MIs was investigated by Tollan et al. (2019). These authors determined that H_2O and CO_2 contents in the colourless MIs range from 2.8–2.9 wt.% and from 332–416 ppm (n=2), respectively, they ranged from 2.8–3.2 wt.% and 191–319 ppm (n=3) in brown MIs, respectively, and the bubble-bearing MI had 3.7 wt.% H_2O and 68 ppm CO_2. In the present study, no additional H_2O and CO_2 in glassy MIs was determined.

The FTIR spectra of quartz from the flow pumice sample are typical for magmatic quartz, with the absorbance dominated by bands centred at 3373 cm^{-1} and 3294 cm^{-1}. These features are interpreted to reflect H charge balancing Al (Stalder and Konzett, 2012). Single point measurements reveal that, for the flow pumice sample, crystal cores contain an average of 5 ± 1

ppm H_2O and rims have an average of 3 ±1 ppm H_2O. Almost all of this difference in absorption is accounted for by the decreased intensity of the band at 3373 cm^{-1} (factor of 3 reduction in integrated absorbance at the rim), while the 3294 cm^{-1} band only shows a factor of 1.3 reduction at the rim, despite being typically considered as part of the same crystallographic defect (Stalder and Konzett, 2012). The high-resolution FPA FTIR images and profiles of host quartz from the flow pumice sample (Fig. 5A–B) confirm a strong, systematically decreasing H_2O towards the crystal rims (i.e., over the outermost 450–600 µm of the crystal). Notably, this does not appear to follow a simple error function shape, indicating that the decrease may not be related to simple H diffusion. An additional feature revealed by the FPA images is a 10 to 50 µm-thick halo of higher OH-related absorbance around the crystallised MIs (Fig. 5A; Supplementary Table S4 and S6) compared to the absorbance in the core.

----INSERT FIGURE 5 - H_2O concentration in host quartz and glassy melt inclusions ----

4.5. Lithium isotope compositions

The four investigated brown glassy MIs hosted in two quartz grains have δ^7Li values from −7.1 ± 1.2‰ to +2.8 ± 1.3‰ (n = 7, n including multiple analyses per inclusion). The single analysed bubble-bearing glassy MI falls in the same range (−7.1 ± 1.5‰). The 38 studied colourless glassy MIs hosted in 19 quartz crystals display a larger, yet overlapping spread of Li isotopic compositions (δ^7Li from −8.0 ± 1.6‰ to +12.3 ± 1.2‰; n = 58, n including multiple analyses per inclusion). For 13 out of 43 glassy MIs, at least two measurements were obtained and show that the Li isotopic composition may vary within a single inclusion. In eight inclusions, δ^7Li values of the rims are between 2.1‰ and 7.2‰ lower compared to the cores. Two inclusions show

no significant internal δ^7Li variations within the analytical uncertainties. Three inclusions have isotopically heavier rims compared to their cores, with the δ^7Li difference from 2.1‰ to 3.5‰. Despite these differences, the range of δ^7Li values obtained in all rims, on one hand, and all cores on the other hand, overlap. The δ^7Li values for rims range from −7.4 ± 1.3‰ to +12.3 ± 1.2‰ whereas the δ^7Li values for all cores range from −8.0 ± 1.6‰ to +12.0 ± 1.3‰. No δ^7Li data for crystallised MIs are presented as there is no SIMS reference material that can reliably be applied to a multi-phase matrix.

The δ^7Li of the groundmass glass from the flow pumice sample varies from +9.4 ± 0.7‰ to +20.5 ± 0.7‰ (average: 15.6‰; n = 42). In the basal pumice sample, the Li isotopic variation of the groundmass glass is smaller (+9.0 ± 1.6‰ to +14.9 ± 1.4‰; average: 12.0‰; n = 14), but overlapping that of the flow pumice sample. Therefore, the total difference in Li isotopic composition between glassy MIs and groundmass glass ($\Delta^7Li_{MI-glass}$) is up to −29‰ for the flow pumice sample and up to −23‰ for the basal pumice sample (Fig. 6). No correlation was found between Li isotopic composition and textural position of the analytical spot within the groundmass glass (i.e., relative distance to, and size of, the nearest vesicles or crystals).

The average δ^7Li values of the groundmass glass that were measured using SIMS (+14.9‰ to +15.6‰; this study) are in apparent disagreement with the published δ^7Li values measured in bulk samples using MC-ICPMS (+6.5‰ to +7.5‰; Neukampf et al. 2019). This discrepancy might result from the bulk glass fraction dissolved for MC-ICPMS analysis containing minor amounts of other mineral phases (e.g., feldspar). This could lower the average δ^7Li value, as these phases are all isotopically lighter than the groundmass glass (Neukampf et al., 2019). This also explains the differences in the Li concentrations of the glass between MC-ICPMS and LA-ICPMS analyses noted by Neukampf et al. (2019).

444

445 ----INSERT FIGURE 6 Li isotopic composition ----

446

447 *5. Discussion*

448 A key finding of this work is the extreme range of δ^7Li between individual quartz-hosted glassy
449 MIs (about 20‰), and between MIs and groundmass glass ($\Delta^7Li_{MI-glass}$ from −23 to −29‰), in the
450 two investigated pumice samples from MFT. Similar Li isotopic heterogeneity has been found in
451 previous studies, which focused on arc magmas. Gurenko et al. (2005) investigated the Li
452 systematics of MIs (Li = 20–60 ppm, δ^7Li from +4‰ to +15‰) in plagioclase and orthopyroxene
453 from a dacitic pumice (Plat Pays Volcanic Complex, Dominica, Lesser Antilles). Bouvier et al.
454 (2010) reported on an even larger range in Li elemental and isotopic composition (Li = 1.1–12
455 ppm, δ^7Li from −24‰ to +8.2‰) for mafic olivine-hosted MIs from basaltic lavas (Grenada
456 Island, Lesser Antilles). Likewise, Kobayashi et al. (2004) analysed olivine-hosted MIs from
457 Hawaiian lavas and revealed δ^7Li variations from −10.2‰ to +8.4‰. In contrast, Schiavi et al.
458 (2012) described a significantly reduced range in Li isotopic composition (δ^7Li from −1.7‰ to
459 +2.3‰) for mafic olivine-hosted MIs from a basaltic lava (San Bartolo, Stromboli, Italy).
460 These studies mostly suggested the observed δ^7Li range by variable contribution of distinct
461 sources, namely slab-derived fluids, sediments, and pristine or metasomatised mantle (Kobayashi
462 et al., 2004; Schiavi et al., 2012). Previous isotopic work on the Yellowstone eruptive rocks also
463 highlighted multiple source components in the mantle and lower to upper crust (Doe et al., 1982;
464 Hildreth et al., 1991; Jean et al., 2014; Wotzlaw et al., 2015), as well as the potential influence of
465 the Farallon slab (Swallow et al., 2018). The largest isotopic contrasts have been observed between
466 the different igneous units of the Snake River Province, while the Yellowstone rhyolites have

relatively homogeneous isotopic compositions (Hildreth et al., 1991; Jean et al., 2014). Moreover, the MFT pumices show very homogeneous major and trace element compositions of groundmass glass and crystals (Neukampf et al., 2019). These observations imply that even if multiple sources are involved, thorough mixing during magma genesis may lead to a Li-homogeneous parental magma for the MFT. In this context, preserving source-related δ^7Li variations in excess of 20‰ is unlikely, especially considering how rapidly Li diffuses in silicic melts (Richter et al., 2009; Holycross et al., 2018).

In the following, we discuss five alternative explanations to source heterogeneity in light of the other observations, notably the variations of Li and H_2O contents in host quartz and MIs.

5.1 Evidence for degassing-driven Li and H_2O diffusion in MFT quartz

Quartz from the two studied samples shows significant intra- and inter-crystal variations in Li contents (Fig. 7), whereas the concentrations of other elements are more homogeneous (Figs. 4 and 7). In particular, the Al concentrations of the quartz crystals from basal pumice (Al = 88–117 ppm) and flow pumice (Al = 93–147 ppm) from the MFT are mostly overlapping. The main mechanism of Li incorporation in quartz is assessed through coupled substitution with Al ($Si^{4+} \leftrightarrow Al^{3+}+Li^{+}$; Denen, 1966; Perny et al., 1992). However, as previously shown (e.g., Audétat and Günther, 1999; Peterková and Dolejš, 2019; Jollands et al. 2020) this substitution may involve other monovalent cations that can compete with Li in this reaction. One of these other cations is possibly H^+, as supported by the different H_2O concentrations of quartz from the two samples: the Li-poorer quartz from the basal pumice shows indeed higher H_2O contents (17 ± 6 ppm; Tollan et al., 2019) than the Li-richer quartz from the flow pumice (5 ± 1 ppm as obtained here). This potentially competing role of H is supported by comparing Li and Al concentrations with the

isoatomic Li:Al 1:1 line (Fig. 7A). All MFT quartz plot in the Al-excess region, indicating that solely Li is insufficient to charge balance Al. Including H reduces the charge deficit substantially (Fig. 7B): the atomic sum of monovalent cations between the two samples is much more similar once H is included (<10% difference) compared to considering Li only (80–90% difference). This indicates that H and Li are indeed both charge-compensating Al and explains the differences in Li concentration between quartz from both samples.

However, even considering H in addition to Li does not entirely charge balance Al (Fig. 7B). This has previously been observed by Jollands et al. (2020), who proposed four possible explanations: (1) inaccurate H_2O analyses using FTIR due to a wrong H absorption coefficient and/or a baseline subtraction routine; (2) inaccurate Li and/or Al concentrations obtained using LA-ICPMS; (3) the presence of other charge-compensators that are not considered (e.g., phosphorus); and (4) incomplete charge balancing of Al. Assuming that our analyses are accurate (which for LA-ICPMS is ensured by the results of the quartz secondary reference material; Supplementary Table S8), the Al excess thus most likely results from other charge-compensating elements that are not considered here, pointing to more complex substitution reactions in quartz (e.g., Peterková and Dolejš, 2019). Nevertheless, this effect has a minor influence compared to the charge balancing effect from H, which clearly has an important effect on the capacity of quartz to incorporate Li (and vice versa).

----INSERT FIGURE 7- Li concentration in host quartz ----

The reason for different relative concentrations of Li and H between the two samples can be further investigated through the study of intra-grains variations. Tollan et al. (2019) imaged the

distribution of H_2O in quartz grains from the basal pumice sample. They described a steeper inwards increase in H in the outermost rim (in the first 200 µm) of the crystals. In comparison, two quartz crystals from the flow pumice sample analysed during the present study show a larger increase in the H_2O content from 450 to 600 µm inwards until reaching a plateau in the core. The intra-grain variations in H_2O contents are not systematically correlated to variations in Al concentrations, which happen at different length scales and/or in opposite directions as expected from substitution laws (Fig. 4C–D). However, they are well correlated to Li concentration profiles. Indeed, quartz from the basal pumice sample, only shows a small inwards decrease in Li content within the outermost rim (Fig. 4F), whereas Li in quartz from the flow pumice sample shows more pronounced zoning, extending over a larger distance from the rim (Fig. 4E).

One possible hypothesis to explain the observed Li and H_2O concentration profiles involves variations in melt composition during quartz crystallisation, as a result of differentiation or magma mixing. A rim-ward increase of Li concentrations could reflect Li enrichment in the melt due to the incompatible character of Li in mineral phases present in MFT (Neukampf et al., 2019). However, this would also be recorded in co-crystallised plagioclase and sanidine (cf. Neukampf et al., 2019; Ellis et al., 2022), whilst their Li systematics rather hint at a rim-ward decrease of Li content (Neukampf et al., 2021). As discussed earlier, this would almost certainly require an unreasonable extent of melt differentiation. Moreover, the crystallisation of the anhydrous mineral assemblage of the MFT would lead to an increase of H_2O in the melt during differentiation, with a rim-ward increase of H_2O content in quartz, exactly opposite to the observed decrease. Magma mixing with a compositionally different melt resulting from magma recharge or cumulate melting can also be excluded. The groundmass glass, MIs and mineral phases from both samples show very similar and homogeneous major–trace element compositions.

Alternatively, changes in the physical–chemical parameters of a volatile phase coexisting with quartz and melt may explain the Li–H systematics in MFT quartz. Charlier et al. (2012) reported on a rim-to-core decrease of Li contents in feldspar and quartz from the rhyolitic Oruanui super eruption (Taupo, New Zealand) and explained this feature by Li re-partitioning from fluid into the melt due to the extraction of chloride into a co-existing vapour phase. Fluxing of an Li-rich volatile phase described for Mount St. Helens (Berlo et al., 2004; Kent et al., 2007; Rowe et al., 2008), or Li-rich gas accumulation as described for the Stromboli volcano (Viccaro et al., 2021), can also lead to an increase of Li concentration in the rims of co-existing minerals. However, all of these processes can be excluded, because they would again lead to Li-enriched rims not only in quartz but also in the co-crystallised feldspar, in contrast to the observations (Neukampf et al., 2021).

Neukampf et al. (2021) proposed that the Li concentration profiles in MFT plagioclase result from diffusive re-equilibration with Li-depleted melt as a result of pre-eruptive degassing. This process would also impoverish the melt in H_2O and by inference, trigger diffusive H^+ loss from crystal rims. In plagioclase, Li and H loss can be readily compensated by limited Na and K diffusion or, to a lesser extent, by the oxidation of multivalent cations such as Fe (Tollan et al., 2018). All of these elements occur in quartz in much lower concentrations than Li and H. Therefore, when H^+ is lost from the host quartz, the most plausible charge balancing substitution is the incorporation of Li^+, especially given that both elements have very similar diffusivities (Jollands et al., 2020). Diffusive loss of H^+ due to melt degassing not only explains the complementary Li–H concentration profiles in MFT quartz, but also the fact that these profiles have different shapes between the two samples. The early erupted basal pumice sample would have indeed experienced a lower degree of degassing relative to the late erupted flow pumice

558 sample, resulting in H^+–Li^+ exchange affecting only the outermost rim (<200 µm) of quartz
559 crystals vs. a thicker rim zone (450–600 µm), respectively.
560 It must be noted, however, that post-eruptive cooling of the ignimbrite deposits could also account
561 for H_2O loss from quartz crystals (Biró et al., 2017) and related Li enrichment via substitution
562 (Ellis et al., 2018). However, no microlite growth in the groundmass glass was observed in any of
563 the two samples which would be indicative of a protracted cooling. Biró et al. (2017) investigated
564 the stratigraphic variations of hydroxyl defects in quartz crystals in thick ignimbrite deposits from
565 N Hungary and showed that the corresponding H_2O concentration decreases from ~12 ppm at the
566 base to ~3 ppm at 6.5–10 m above the base, with a more abrupt decrease in the case of welded
567 deposits. However, both of our samples were collected ca. 2 m apart from the non-welded part of
568 the deposit, respectively from the fallout below the base for the basal pumice; and the basal part
569 of the MFT for the flow pumice. Therefore, our samples correlate to the lowermost parts of the
570 deposits investigated by Biró et al. (2017), which experienced the lowest amount of post-
571 depositional H diffusion. In addition, Biró et al. (2017) modelled post-depositional dehydration
572 across the deposit via diffusional loss over a range of temperatures (300-700°C) and found that
573 contrasting cooling rates and different crystal sizes do not account for the observed H_2O
574 concentration profiles. They concluded that other factors like magma chamber zoning and the pre-
575 depositional thermal history also influence the distribution of H_2O concentrations in quartz crystals
576 from ignimbrite deposits, as argued here.
577 Collectively, we interpret the Li and H_2O zoning of quartz from the two samples, and the
578 different shapes of the resulting concentration profiles between them, as a result of different
579 timescales and/or extents of pre-eruptive degassing.
580

5.2. Effects of degassing on Li and H_2O in melt inclusions

Having established that degassing controls the Li and H_2O systematics of the host quartz from the two samples, we now address how MIs may reveal more details on the pre- and syn-eruptive volatile behaviour of the MFT magma system.

Strikingly, the two samples show different MI types: mostly glassy in the basal pumice vs. mostly partly crystallised in the flow pumice. In addition, crystallised MIs show higher average Li contents relative to the glassy ones (Fig. 3A). We postulate that in the flow pumice sample, diffusive H_2O loss from the MI would have potentially triggered the crystallisation of the MIs. In mafic melts and minerals (e.g., olivine-hosted MIs), this process is generally associated with Fe oxidation (Danyushevsky et al., 2002; Gaetani et al., 2012), but due to the low Fe contents of both quartz and high-silica rhyolitic MIs in the case of the MFT, this is likely compensated by inward Li diffusion to ensure charge balance. Moreover, outward diffusion of H_2O from the MI would explain the "halo" of increased H_2O concentration surrounding crystallised MIs in the host quartz (Fig. 5A).

This explanation is supported by the experimental results of Zajacz et al. (2009), who determined that MIs can suffer post-entrapment modification of trace element contents due to the in- and outward migration of molecular H_2 and H_2O resulting from a concentration gradient at temperatures and pressures typical for upper crustal felsic magma storage. This gradient can result in a rapid diffusion of H^+, Li^+ and Na^+ parallel to the *c*-axis in quartz that needs to be charge balanced (e.g., Audétat and Günther, 1999, Rottier et al., 2017). Other experiments showed that H-bearing species (OH^-, H_2O) can diffuse through the host quartz as a result of the pressure gradient that the MIs experience (Qin et al., 1992; Severs et al., 2007), i.e., during the ascent of the magma. In the case of Yellowstone, this process has been proposed as an explanation for the

spread in H_2O concentrations of MIs from the Huckleberry Ridge Tuff (HRT; 0.5–4.5 wt.%; Fig. 5C and D) (Myers et al., 2016), suggesting in turn that some MIs potentially lost up to ~80% of their original H_2O concentration (Myers et al., 2019).

In the case of the MFT samples, loss of H_2O from crystallised MI is apparently in contradiction with their similar H_2O and CO_2 concentrations (2.2–3.8 wt.% and 120–470 ppm respectively, as estimated here) to those of the glassy MIs (2.8–3.7 wt.% and 68–416 ppm, respectively; Tollan et al., 2019). However, loss of up to a few thousand ppm H_2O from MIs, which is well within the error of the FTIR measurements (about ± 0.4 wt.%), would be sufficient to explain the "halo" of increased H_2O concentration surrounding crystallised MIs in the host quartz. Therefore, compared to the quartz-hosted MIs from the HRT, those of the MFT have lost a smaller fraction of their H_2O budget, i.e., a maximum of 30% (~1 wt.%, corresponding to the observed concentration range). This presumably results from the less complex magmatic history of the MFT compared to that of the HRT. Considering the experimental results (e.g., Qin et al., 1992; Severs et al., 2007), we advocate for equilibration of the host quartz with its surrounding melt during ascent, which then also affects the MIs. As proposed to explain the Li–H_2O concentration profiles in the host quartz, pre-eruptive degassing would deplete the surrounding melt in H_2O, thereby producing the chemical gradient required for the diffusive loss of H species from MIs. In accord with the differences in quartz concentration profiles, longer and/or more pronounced degassing in the case of the later erupted flow pumice explains that this sample contains mostly crystallised MIs, whereas the early erupted basal pumice contains mostly glassy MIs. This process can further explain the zonation in Li concentration and δ^7Li in the glassy MIs in the basal pumice sample. Lithium concentrations and δ^7Li values generally are independent of MI size and the location of the melt inclusion in the crystal. When the glassy MIs experienced diffusive loss of H-bearing species, charge balancing by

Li likely also happened through diffusion insofar both species have similar diffusivities (Jollands et al., 2020). As ^{6}Li diffuses ~3.5% faster compared to ^{7}Li (Parkinson et al., 2007; Richter et al., 2009; Holycross et al., 2018) the rims of the MIs become enriched in ^{6}Li (i.e., isotopically lighter) compared to the cores. From this perspective, cores of glassy MIs potentially represent the least modified sections in terms of Li concentrations and δ^{7}Li values of the melt.

5.3. Kinetic fractionation of lithium isotopes in melt during ascent (open-system degassing)

The groundmass glass from both samples shows a broad negative correlation between δ^{7}Li and Li contents (Fig. 6). During degassing of felsic melts, Li partitions into the immediately formed vapour phase (Webster et al., 1989), so that the melt would become progressively depleted in Li (e.g., Neukampf et al., 2021). If degassing is an open-system disequilibrium process, then this should be accompanied by kinetic Li isotopic fractionation between melt and vapour phase because ^{6}Li moves ~3.5% faster than ^{7}Li (Parkinson et al., 2007; Richter et al., 2009; Holycross et al., 2018). During degassing, the melt will thus acquire a heavier Li isotopic signature. This process would adequately explain the observed co-variation between δ^{7}Li and Li content in groundmass glass, with Li-richer (ca. 45 ppm) and the isotopically lightest (δ^{7}Li of ca. +10‰) glass representing the closest composition to an undegassed melt.

In addition, the Li isotopic composition of the groundmass glass between the two samples varies on average by 3.4‰, with glass from the basal pumice sample (δ^{7}Li = +9‰ to +14.9‰) being isotopically lighter and on average more homogeneous than that of the flow pumice sample (δ^{7}Li = +9.4‰ to +20.5‰) (Fig. 6). This may be explained by the variability in decompression and cooling rates during the eruption, and thus by variability in the efficiency of degassing. We propose

650 that rapid decompression and cooling minimises Li loss by degassing and associated Li isotope
651 fractionation between the formed vapour phase and melt (Ionov and Seitz, 2008), explaining the
652 elemental and isotopic composition of groundmass glass from the basal pumice sample. In
653 contrast, protracted degassing entails more Li moving into the vapour phase, resulting in an
654 isotopically progressively heavier melt with time as recorded by groundmass glass in the flow
655 pumice sample. This would be consistent with the relative timing of eruption between the two
656 samples and the interpretation of the quartz Li–H_2O data discussed above.
657 Alternatively, the Li isotopic variation within the groundmass glass within samples could be
658 explained by different bubble sizes during degassing. Large-sized bubbles would lead to more ^{6}Li
659 diffusing from the melt into the vapour phase, resulting in heavier δ^7Li in the melt, whereas smaller
660 bubbles would lead to a lesser extent of depletion of ^{6}Li in the melt. This has only been
661 theoretically addressed by Watson (2017) and still needs to be assessed experimentally. In any
662 case, we did not observe any correlation between Li isotopic composition of the groundmass glass
663 and the size of the nearest vesicle that would be indicative of this process.
664 Collectively, we propose that Li isotopic variations in the groundmass glass of both samples
665 require disequilibrium (kinetic) open-system degassing occurring over a short period of time and
666 thereby controlled by diffusive kinetic fractionation between ^{6}Li and ^{7}Li. Geospeedometry based
667 on Li elemental and isotopic diffusion profiles in plagioclase indicates that the timescales of such
668 degassing were on the order of tens of minutes (Neukampf et al., 2021), similar to experimental
669 results of Coogan (2011). In turn, preserving the signature of such an open-system, fast
670 fractionation process implies that it is not related to processes taking place in the magma reservoir
671 and, instead, it must have taken place during ascent in the conduit immediately prior to eruption.

It is possible to model the kinetic Li isotopic fractionation during open-system degassing in the conduit using the following equation:

$$(\delta^7Li)_{melt} = [(\delta^7Li)_0 + [((\alpha_{vapour-melt} - 1) \times 1000) \times (\ln(F))],$$

where $(\delta^7Li)_{melt}$ represents Li isotope composition of the degassed melt, $(\delta^7Li)_0$ is the δ^7Li value of the initial magma, $\alpha_{vapour-melt}$ is the bulk Li isotopic fractionation factor between vapour and melt, and F represents the fraction of Li remaining in the melt. The Li concentration in the degassed magma can be calculated following Schiavi et al. (2010):

$$Li_{melt} = Li_0(F^{(D-1)}),$$

where Li_0 is the initial Li concentration, Li_{melt} is the Li concentration after degassing, and D is the bulk distribution coefficient of Li between melt and vapour. To calculate $(\delta^7Li)_{melt}$ and Li_{melt} the parameter $\alpha_{vapour-melt}$ and D need to be determined. In the case of kinetic fractionation, the parameter $\alpha_{vapour-melt}$ can be calculated as $\alpha_{vapour-melt} = \left(m_{^6Li}/m_{^7Li}\right)^{\beta}$ with $\beta = 0.228$ as the empirical constant of the kinetic fractionation of Li isotopes obtained from experiments close to the composition of the MFT melt (Holycross et al., 2018). This results in a value of 0.965 for $\alpha_{vapour-melt}$, consistent with ^{6}Li preferentially fractionating in the vapour phase. This is in good agreement with $\alpha_{vapour-melt}$ established by Beck et al (2004) for Li_2O $\alpha_{vapour-melt} = 0.966$ and Li_2S $\alpha_{vapour-melt} = 0.978$. Koga et al. (2008) showed, based on experiments using mass balance, that $D_{vapour-melt}$ should be between 1 and 30. Here, all values $D > 3$ fail to explain our data and are, therefore, not displayed. To estimate the best fitting $D_{vapour-melt}$ a range from 1 to 3 with different

$\alpha_{vapour–melt}$ (0.965 and 0.978) were tested. We used $(\delta^7Li)_0$ = 9.4‰ and [Li] = 46.3 ppm as a plausible starting composition, reflecting a melt present in the MFT reservoir, and not yet affected by conduit degassing (Fig. 8A). Both $\alpha_{vapour–melt}$ values (0.965 and 0.978) can explain the kinetic fractionation observed within the samples (Fig. 8A). Best fits are obtained for a $D_{vapour–melt}$ = 1.5 when considering an $\alpha_{vapour–melt}$ = 0.965, and for a $D_{vapour–melt}$ = 2 when considering an $\alpha_{vapour–melt}$ = 0.978. Only 30% (F = 0.7) degassing is required to fractionate Li to obtain the high δ^7Li values that were measured in the groundmass glass. Therefore, the model of open-system degassing with disequilibrium kinetic fractionation of the Li isotopes appears to successfully explain the data distribution. As both samples have a wide range in δ^7Li values and Li concentrations it is possible that Li is degassing as Li_2O and Li_2S; LiCl is not considered because no experimental data is yet available for $\alpha_{vapour–melt}$ and $D_{vapour–melt}$ although we posit that LiCl may be an important species during degassing.

----INSERT FIGURE 8 Li isotopic composition model----

5.4. Fractionation of lithium isotopes in the magma reservoir as recorded in melt inclusions

The kinetic fractionation that takes place during degassing in the conduit explains the variations in Li and H_2O concentrations in the host quartz between the two samples; the zoning in Li in MIs; and the differences in Li contents and isotopic compositions between groundmass glass of the two samples. However, it cannot explain the large variation in δ^7Li and Li contents in MIs between different grains of the same sample. Different MIs measured within one grain show limited variations in δ^7Li and Li contents compared to the overall variation of the entire population,

718 indicating that they sample a compositionally uniform melt and possibly were trapped within a
719 short period of time. As there is no relationship between δ^7Li, the size of MIs and their position
720 relative to the rim of the quartz crystals (Fig. 6), post-entrapment diffusive loss of Li has to be
721 excluded. Furthermore, contrary to what is observed for the groundmass glass, there is a broad
722 positive correlation between Li and δ^7Li (Fig. 6). Therefore, we must consider that the groundmass
723 glass and the MIs represent melts that were sampled from different parts and/or evolutionary stages
724 of the magmatic system. Likewise, a distinct process occurring within the magma reservoir, i.e.,
725 taking place together with quartz crystallisation and related entrapment of MIs, must be
726 responsible for the δ^7Li and Li content variations of MIs.

727 The pre-eruptive evolution of the magma reservoir parental to the MFT involved several
728 successive magma injections as well as the co-existence of crystal-poor vs. crystal-rich domains,
729 as demonstrated by the relationships between high-precision zircon U–Pb ages and trace element
730 concentrations (Rivera et al., 2016). Like zircons, the MFT quartz phenocrysts containing the MIs
731 likely derived from these different regions of the magmatic reservoir. In particular, we postulate
732 that the mushy domains, such as marginal granophyric rinds, were disaggregated during the
733 eruption and sampled by crystal-poor rhyolitic magma representing a deeper and hotter part of the
734 reservoir, as proposed for phenocryst-rich pumice clasts in other silicic volcanic units such as the
735 Kos Plateau Tuff (Allen, 2001; Fiedrich et al., 2020). Therefore, it is likely that the MFT quartz
736 phenocrysts grew from a melt, now represented by MIs, that underwent different extents of Li loss
737 through passive degassing within the magma reservoir; whereas the groundmass glass represents
738 "primitive" Li-rich melt that degassed only in the conduit during the eruption. This hypothesis is
739 in good agreement with the fact that the trends defined by the groundmass glass and the MIs

converge at their high-Li end (Fig. 6, Fig. 8), which is likely close to the original composition of the less degassed melt prior to the MFT eruption.

In the following we discuss possible explanations for the observed variations in δ^7Li and Li between the different MIs of MFT.

In our models we assume that Li partitions solely into the formed vapour phase. Lithium partitioning into a non-vapour (i.e., supercritical) fluid phase, though possible (e.g., Iveson et al., 2019), is not considered because the partitioning parameters related to such a process are not yet constrained. For the variations between the MIs, we infer that the magma prior to eruption is degassing in the upper part of the magma reservoir over a longer period of time (days to years), and we therefore consider equilibrium, either open- or closed-system degassing. This means that fractionation between ^{7}Li and ^{6}Li between melt and vapour phase is controlled by equilibrium partitioning rather than diffusive fractionation.

In the case of closed-system degassing the vapour-hosted Li can still exchange with the melt. This can be calculated using the following equations:

$$(\delta^7Li)_{magma} = \delta^7Li_0 - [(1-F)\times10^3\times ln\alpha_{vapour-melt}],$$

and

$$Li_{magma} = Li_0 /[(1- D_{vapour-\ melt})\times F + D_{vapour-melt}],$$

where $(\delta^7\text{Li})_{\text{magma}}$ represents Li isotope composition of the degassed magma, and $(\delta^7\text{Li})_0$ is the δ^7Li value of the initial magma. The parameter $\alpha_{vapour-melt}$ has not yet been determined

763 experimentally in the case of Rayleigh distillation for this melt composition and the relevant
764 temperature and pressure conditions. Previous studies have used $\alpha_{vapour-melt}$ = 1.0100 or 1.0099
765 (Vlastélic et al., 2011) and $\alpha_{vapour-melt}$ = 1.005 to 1.015 (Schiavi et al., 2010). As they are the best
766 estimates available so far, we have explored this range of $\alpha_{vapour-melt}$ in the model. Concerning
767 $D_{vapour-melt}$, we used the range determined in section 5.3 ($D_{vapour-melt}$ = 1–3) as the best proxy for
768 the considered rhyolite compositions. For $(\delta^7Li)_0$ and Li_0 we assumed that the highest δ^7Li values
769 with the highest Li concentration measured in the cores of the MIs represent the least modified
770 pre-eruptive composition of the melt. Accordingly, two starting points for the model where chosen:
771 (1) the highest Li concentration in a MI ($[\delta^7Li]_0$ = 9.9‰; Li_0 = 59.9 ppm), and (2) the heaviest Li
772 isotopic composition ($[\delta^7Li]_0$ = 12‰; Li_0 = 51.4 ppm). Figure 8D shows the results for $\alpha_{vapour-melt}$
773 = 1.005, 1.010 and 1.015 and with $D_{vapour-melt}$ = 2. When assuming up to 100% (F = 0) degassing
774 and using $\alpha_{vapour-melt}$ equal to 1.005, δ^7Li values are fractionated by 5‰, for $\alpha_{vapour-melt}$ equal to
775 1.010, δ^7Li is fractionated by up to 9‰, and for $\alpha_{vapour-melt}$ equal to 1.015 up to 14‰ change is
776 modelled for $^7Li/^6Li$. All modelled fractionation curves fail to explain the isotope data as they
777 cannot explain the lightest δ^7Li values (< −2.5‰) and only lead to a small change in Li
778 concentration. Therefore, closed-system degassing is excluded as a possible explanation for the
779 MI data.

780 Another possibility is open-system degassing taking place in the magma reservoir (Fig. 9),
781 assuming equilibrium fractionation. Therefore, the simple Rayleigh distillation law can be applied:
782

783 $$(\delta^7Li)_{magma} = [(\delta^7Li)_0+1000]F^{\alpha-1}-1000,$$

784

and residual Li concentration in the magma can be calculated following Schiavi et al. (2010):

$$Li_{residual} = Li_0(F^{(D-1)}),$$

where Li_0 is the initial Li concentration, and Li_{residual} is the Li concentration after degassing. We applied the same values for δ^7Li_0, F, D and $\alpha_{vapour-melt}$ as for the closed-system degassing model above. In figure 8B only one starting point is used to estimate the best fitting $D_{vapour-melt}$ ($D_{vapour-melt}$ = 1.5 to 3) whereby $D_{vapour-melt}$ = 2 yields the best fit to the data set; other D values resulted in a strong misfit. Figure 8C highlights that the best fit is achieved when using $\alpha_{vapour-melt}$ = 1.010 (with $D_{vapour-melt}$ = 2). Our results show that up to 85% (F = 0.15) of Li degassing is required to account for the lightest δ^7Li. Thus, our model for open-system degassing in the magma reservoir successfully explains the data distribution observed for δ^7Li between different MIs.

Although open-system Rayleigh fractionation explains most of the data, there is residual scatter that cannot be accounted for by this model. It is therefore possible that other processes are superimposed on those resulting from degassing, e.g., fractional crystallisation that simultaneously takes place during MI entrapment. An alternative explanation is a multistage ascent within a magma reservoir, whereby the isotopically lightest melt inclusions were trapped first, and during continuous loss of ^{6}Li via degassing, the melt and trapped MIs became isotopically heavier. However, this is not supported by the Li concentration of the MIs as the concomitant increase would require more than 50% of crystal fractionation (unsupported by other geochemical evidence) to reach the Li concentration of the groundmass glass and the highest Li concentrations in the MIs.

6. Conclusion

The main conclusions reached in this study are:

(1) Quartz-hosted MIs in pyroclastic deposits from the MFT are heterogeneous in δ^7Li composition (from −8.0‰ to +12.3‰) and Li concentration (10–61 ppm), as a result of variable extents of equilibrium open-system degassing of rhyolitic melt at depth in the magma reservoir, over long timescales (days to years) prior to eruption (Fig. 9A).

(2) During melt ascent within tens of minutes (Neukampf et al., 2021) prior to eruption, the Li and H_2O composition of host quartz is modified by diffusive exchange between degassing melt and quartz, with Li charge balancing the outward diffusion of the different H species from the quartz (Fig. 9B-D).

(3) Some rims of the MIs are modified post entrapment by diffusional exchange between host quartz and MIs during the ascent. Therefore, only the cores of some MIs preserve the least modified pre-eruptive Li concentration and δ^7Li values of the MFT magma reservoir.

(4) Degassing in the conduit occurred as an open-system disequilibrium process, which led to kinetic fractionation of Li isotopes between melt and vapour phase with ^{6}Li preferentially fractionating into the vapour phase (Fig. 9B–D), resulting in higher δ^7Li values and lower Li concentrations of groundmass glass.

(5) Different timescales and/or extents of degassing resulted in more pronounced chemical and isotopic exchange between quartz, MIs, melt and vapour (Fig. 9C–D), as recorded by the later erupted flow pumice sample. Further kinetic fractionation between melt and vapour resulted in the negative correlation between δ^7Li and Li contents of

groundmass glass. The diffusive Li–H_2O exchange in quartz affected larger distances from the crystal rims; simultaneously, H_2O is lost from the MIs leading to their crystallisation and Li enrichment due to charge balance.

----INSERT FIGURE 9 Comic----

This study shows that particular attention should be exercised with regard to the selection of MIs for geochemical analyses, especially when Li is considered. Our data shows that degassing processes alone, both at depth prior to eruption and happening rapidly in the conduit during eruption, can result in a substantial variability of δ^7Li (up to nearly 30‰) in melts and resulting MIs/groundmass glass. Therefore, Li isotopic compositions of MIs should be used with great caution when applied directly as a proxy to track changes in the melt. To discuss source characteristics, it is therefore important to conduct a comprehensive study of MIs and apply Li isotopes in tandem with other isotope systems that are unaffected by degassing at depth and in the conduit. However, we posit that Li can provide important information regarding pre- and syn-eruptive degassing in silicic volcanic systems. The combination of Li concentration, *in situ* δ^7Li measurements in quartz-hosted MIs and groundmass glass and diffusion modelling of Li concentration gradients in quartz potentially represents a powerful tool to understand late-stage magmatic processes.

Acknowledgements

We thank Julien Allaz for his help during electron probe analyses, Marcel Guillong for his help during LA-ICPMS analyses and Colin Macpherson for fruitful discussions. This work was

854 supported by the Swiss National Science Foundation grant 200021_166281 to BE. TM contributed
855 through the Czech Science Foundation project 19-29124X. This work was supported by the French
856 National Research Agency through the national program “Investissements d'avenir” with the
857 reference ANR-10-LABX-21-01/LABEX RESSOURCES21 to JN and LF. The manuscript
858 benefited from detailed reviews by Madison Myers and two anonymous reviewers. Rosemary
859 Hickey-Vargas and Jeffrey Catalano are acknowledged for editorial handling.

Appendix A. Supplementary Material

The supplementary data file includes the major- and trace element composition as well as the δ^7Li composition of groundmass glass and quartz-hosted melt inclusions from the two samples (basal and flow pumice sample) used in this study. In the supplement file the basal pumice sample is referred to as 11022 and the flow pumice samples as 13005. Additionally, the trace element composition of the quartz crystals that hosted the melt inclusions are given as well as their H_2O concentration and FTIR maps. The secondary standards used during major- and trace element as well as lithium isotope measurements are provided.

References

Allen S. R. (2001) Reconstruction of a major caldera-forming eruption from pyroclastic deposit characteristics: Kos PlateauTuff, eastern Aegean Sea. *J. Volcanol. Geoth. Res*. **105**, 141–162.

Audétat A. and Günther D. (1999) Mobility and H_2O loss from fluid inclusions in natural quartz crystals. *Contrib. Mineral. Petrol.* **137**, 1–14.

Audétat A., Garbe-Schönberg D., Kronz A., Pettke T., Rusk B., Donovan J. J., Lowers H. A. (2015) Characterisation of a natural quartz crystal as a reference material for microanalytical determination of Ti, Al, Li, Fe, Mn, Ga and Ge. *Geostand. Geoanal. Res.* **39** (2), 171–184.

Beinlich A., John T., Vrijmoed J.C., Tominaga M., Magna T., Podladchikov Y. Y. (2020) Instantaneous rock transformations in the deep crust driven by reactive fluid flow. *Nat. Geosci.* **13**, 307–311.

Behrens H., Tamic N., Holtz F. (2004) Determination of the molar absorption coefficient for the infrared absorption band of CO_2 in rhyolitic glasses. *Am. Mineral.* **89**, 301–306.

Benson T. R., Coble M. A., Rytuba J. J., Mahood G. A. (2017), Lithium enrichment in intracontinental rhyolite magmas leads to Li deposits in caldera basins. *Nat. Commun*. **8**, 270.

Berlo K., Blundy, J., Turner, S., Cashman, K., Hawkesworth, C., Black S. (2004) Geochemical precursors to volcanic activity at Mount St. Helens, USA. *Science* **306**, 1167−1169.

Biró T., Kovács I. J., Karátson D., Stalder R., Király E., Falus G., Fancsik T., Sándorné J. K. (2017) Evidence for post-depositional diffusional loss of hydrogen in quartz phenocryst fragments within ignimbrites, *Am. Mineral.* **102**, 1187–1201.

889Bouvier A.-S., Métrich N., Deloule E. (2008) Slab-derived fluids in magma sources of St. Vincent
890 (Lesser Antilles Arc): volatile and light element imprints. *J. Petrol.* **49** (8), 1427–1448.

891Bouvier A.-S., Métrich N., Deloule E. (2010) Light elements, volatiles, and stable isotopes in basaltic
892 melt inclusions from Grenada, Lesser Antilles: Inferences for magma genesis. *Geochem.*
893 *Geophys. Geosyst*. **11** (9).

894Chan L. H., Edmond J. M. (1988) Variation of lithium isotope composition in the marine environment:
895 a preliminary report. *Geochim. Cosmochim. Acta* **52**, 1711−1717.

896Chan L. H., Edmond J. M., Thompson G., Gillis K. (1992) Lithium isotopic composition of submarine
897 basalts: implications for the lithium cycle in the oceans. *Earth Planet. Sci. Lett.* **108**, 151−160.

898Charlier B., Morgan D., Wilson C., Wooden J., Allan A., Baker J. (2012) Lithium concentration
899 gradients in feldspar and quartz record the final minutes of magma ascent in an explosive
900 supereruption. *Earth Planet. Sci. Lett.* **319–320**, 218−227.

901Christiansen R.L. (2001) The Quaternary and Pliocene Yellowstone Plateau Volcanic Field of
902 Wyoming, Idaho, and Montana. US Geological Survey Professional Paper 729-G.

903Coogan L. A. (2011) Preliminary experimental determination of the partitioning of lithium between
904 plagioclase crystals of different anorthite contents. *Lithos* **125** (1–2), 711–715.

905Danyushevsky L. V., Della-Pasqua F. N., Sokolov S. (2000) Re-equilibration of melt inclusions
906 trapped by magnesian olivine phenocrysts from subduction-related magmas. petrological
907 implications. *Contrib. Mineral. Petrol.* **138**, 68–83.

Danyushevsky L. V., McNeill A. W., Sobolev A. V. (2002) Experimental and petrological studies of melt inclusions in phenocrysts from mantle-derived magmas: an overview of techniques, advantages and complications. *Chem. Geol.* **183**, 5–24.

Denen W. H. (1966) Stoichiometric substitution in natural quartz. *Geochim. Cosmochim. Acta* **30**, 1235–1241.

Doe B. R., Leeman W. P., Christiansen R. L., Hedge, C. E. (1982). Lead and strontium isotopes and related trace elements as genetic tracers in the Upper Cenozoic rhyolite–basalt association of the Yellowstone Plateau Volcanic Field. *J. Geophys. Res. Solid Earth* **87**, 4785–4806.

Elliott T., Thomas A., Jeffcoate A., Niu Y. (2006) Lithium isotope evidence for subduction-enriched mantle in the source of Mid-Ocean-Ridge Basalts. *Nature* **443** (7111), 565–568.

Ellis B. S., Wolff J. A., Boroughs S., Mark D. F., Starkel W.A., Bonnichsen B. (2013) Rhyolitic volcanism of the central Snake River Plain: A review. *Bull. Volcanol.* **75** (8), 745.

Ellis B.S., Mark D.F., Troch J., Bachmann O., Guillong M., von Kent A.J.R., Quadt A. (2017) Split-Grain 40Ar/39Ar dating: integrating temporal and geochemical data from crystal cargoes. *Chem. Geol.* **457**, 15−23.

Ellis B.S., Szymanowski D., Magna T., Neukampf J., Dohmen R., Bachmann O., Ulmer P., Guillong M. (2018) Post-eruptive mobility of lithium in volcanic rocks. *Nat. Commun.* **9**, 3228.

Ellis B.S., Szymanowski D., Harris C., Tollan P.M.E., Neukampf J., Guillong M., Cortes-Calderon E.A., Bachmann O. (2021) Evaluating the potential of rhyolitic glass as a lithium source for brine deposits. *Econ. Geol.*, 117 (1), 91-105.

928Ellis B.S., Neukampf J., Bachmann O., Harris C., Forni F., Magna T., Laurent O., Ulmer P. (2022)
929 Biotite as a recorder of an exsolved Li-rich volatile phase in upper crustal silicic magma
930 reservoirs. *Geology*, Doi: 10.1130/G49484.1.

931Flesch G. D., Anderson Jr. A. R., Svec H. J. (1973) A secondary isotopic standard for $^{6}Li/^{7}Li$
932 determinations. *Int. J. Mass Spectrom. Ion Phys.* **12** (3), 265–272.

933Frezzotti M.L. (2001) Silicate-melt inclusions in magmatic rocks: applications to petrology. *Lithos* **55**,
934 273–299.

935Fiedrich A.M., Laurent O., Heinrich C.A., Bachmann O. (2020) Melt and fluid evolution in an upper-
936 crustal magma reservoir, preserved by inclusions in juvenile clasts from the Kos Plateau Tuff,
937 Aegean Arc, Greece. *Geochim. Cosmochim. Acta* **280**, 237–262.

938Gaetani G.A., O'Leary J.A., Shimizu N., Bucholz C.E., Newville M. (2012) Rapid reequilibration of
939 H_2O and oxygen fugacity in olivine-hosted melt inclusions. *Geology* **40**, 915-918.

940Giuffrida M., Viccaro M., Ottolini L. (2018) Ultrafast syn-eruptive degassing and ascent trigger high-
941 energy basic eruptions. *Sci. Rep.* **8** (1), 147.

942Guillong M., Meier D.K., Allan M.M., Heinrich C.A., Yardley B.W.D. (2008) SILLS: A Matlab-
943 Based Program for the Reduction of Laser Ablation ICP–MS Data of Homogeneous Materials
944 and Inclusions. Mineralogical Association of Canada Short Course, Vancouver, B.C **40**, 328–
945 333.

946Gurenko A. A., Trumbull R. B., Thomas R., Lindsay J. M. (2005) A melt inclusion record of volatiles,
947 trace elements and Li – B isotope variations in a single magma system from the Plat Pays
948 Volcanic Complex, Dominica, Lesser Antilles. *J. Petrol.* **46**, 2495–2526.

949Hildreth W., Halliday A. N., Christiansen, R. L. (1991). Isotopic and chemical evidence concerning
950 the genesis and contamination of basaltic and rhyolitic magma beneath the Yellowstone
951 Plateau volcanic field. *J. Petrol.* **32**, 63–138.

952Hofstra A. H., Todorov T. I., Mercer C. N., Adams D. T., Marsh E. E. (2013) Silicate Melt Inclusion
953 Evidence for Extreme Pre-eruptive Enrichment and Post-eruptive Depletion of Lithium in
954 Silicic Volcanic Rocks of the Western United States: Implications for the Origin of Lithium-
955 Rich Brines. *Econ. Geol.*, **108**, 1691−1701.

956Holycross M. E., Watson E. B., Richter F. M., Villeneuve J. (2018) Diffusive fractionation of Li
957 isotopes in wet, silicic melts. *Geochem. Perspect. Lett.* **6**, 39-42.

958Hoover W. F., Penniston-Dorland S. C., Baumgartner L. P., Bouvier A.-S., Baker D., Dragovic B.,
959 Gion A. (2021) A Method for Secondary Ion Mass Spectrometry Measurement of Lithium
960 Isotopes in Garnet: The Utility of Glass Reference Materials. *Geostand. Geoanal. Res.* **45**, 477-
961 499.

962Humphreys M., Menand T., Blundy J.D., Klimm K. (2008) Magma ascent rates in explosive eruptions:
963 constraints from H_2O diffusion in melt inclusions. *Earth Planet. Sci. Lett.* **270**, 25–40.

964Ionov D.A., Seitz H.M. (2008) Lithium abundances and isotopic compositions in mantle xenoliths
965 from subduction and intra-plate settings: mantle sources vs. eruption histories. *Earth Planet.*
966 *Sci. Lett.* **266**, 316-331.

967Iveson A. A., Webster J. D., Rowe M. C., Neill O. K. (2019) Fluid-melt trace-element partitioning
968 behaviour between evolved melts and aqueous fluids: Experimental constraints on the
969 magmatic-hydrothermal transport of metals. *Chem. Geol.* **516,** 18-41.

970Jackson A., Parker R. L., Sambridge M., Constable C., Wolf A. S. (2018) The inverse problem of
971 unpolarized infrared spectroscopy of geological materials: estimation from noisy random
972 sampling of a quadratic form. *Am. Miner.* **103**,1176–1184.

973Jean M. M., Hanan, B. B., Shervais, J. W. (2014). Yellowstone hotspot–continental lithosphere
974 interaction. *Earth Planet. Sci. Lett.* **389**, 119–131.

975Jeffcoate A. B., Elliott T., Kasemann S. A., Ionov D., Cooper K., Brooker R. (2007) Li isotope
976 fractionation in peridotites and mafic melts. *Geochim. Cosmochim. Acta* **71**, 202−218.

977Jochum K. P., Weis U., Stoll B., Kuzmin D., Yang Q., Raczek I., Jacob D. E., Stracke A., Birbaum
978 K., Frick D. A., Günther D., Enzweiler J. (2011) Determination of reference values for NIST
979 SRM 610–617 glasses following ISO guidelines. *Geostand. Geoanal. Res.* **35**, 397–429.

980John T., Gussone N., Podladchikov Y. Y., Bebout G. E., Dohmen R., Halama R., Klemd R., Magna
981 T., Seitz H-M (2012) Volcanic arcs fed by rapid pulsed fluid flow through subducting slabs.
982 *Nat. Geosci.* **5**, 489−492.

983Johnson E. A., Rossman G. R. (2013) The diffusion behavior of hydrogen in plagioclase feldspar at
984 800–1000 °C: implications for re-equilibration of hydroxyl in volcanic phenocrysts. *Am.*
985 *Mineral.* **98**, 1779−1787.

986Jollands M. C., Ellis B., Tollan P. M. E., Müntener O., (2020) An eruption chronometer based on
987 experimentally determined H-Li and H-Na diffusion in quartz applied to the Bishop Tuff, *Earth*
988 *Planet. Sci. Lett.* **551**, 116560.

989Kasemann S.A., Jeffcoate A. B., Elliott T. (2005) Lithium isotope composition of basalt glass
990 reference material. *Analytical Chemistry* **77**, 5251−5257.

991Kent A. J. R., Blundy J., Cashman K. V., Cooper K. M., Donnelly C., Pallister J. S., Reagan M., Rowe
992 M. C., Thornber C. R. (2007) Vapor transfer prior to the October 2004 eruption of Mount St.
993 Helens, Washington. *Geology* **35** (3), 231–234.

994Kobayashi K., Tanaka R., Moriguti T., Shimizu K., Nakamura E. (2004) Lithium, boron, and lead
995 isotope systematics of glass inclusions in olivines from Hawaiian lavas: evidence for recycled
996 components in the Hawaiian plume. *Chem. Geol.* **212** (1), 143−161.

997de León A.C., Schmitt A. K. (2019) Reconciling Li and O diffusion in zircon with protracted magmatic
998 crystal residence. *Contrib. Mineral. Petrol.* **174** (4), 28.

999Lindsay J. M., Schmitt A. K., Trumbull R. B., de Silva S. L., Siebel W., Emmermann R. (2001)
1000 Magmatic evolution of the La Pacana Caldera system, central Andes, Chile: compositional
1001 variation of two cogenetic, large-volume felsic ignimbrites and implications for contrasting
1002 eruption mechanisms. *J. Petrol.* **42**, 459–486.

1003Lloyd A. S., Plank T., Ruprecht P., Hauri E.H., Rose W. (2013) Volatile loss from melt inclusions in
1004 pyroclasts of differing sizes. *Contrib. Mineral. Petrol.* **165**, 129-153.

1005Lundstrom C. C., Chaussidon M., Hsui A.T., Kelemen P., Zimmerman M. (2005) Observations of Li
1006 isotopic variations in the Trinity ophiolite: evidence for isotopic fractionation by diffusion
1007 during mantle melting. *Geochim. Cosmochim. Acta* **69**, 735−751.

1008Lynn K. J., Shea T., Garcia M.O., Costa F., Norman M.D. (2018) Lithium diffusion in olivine records
1009 magmatic priming of explosive basaltic eruptions. *Earth Planet. Sci. Lett*. **500**, 127-135.

1010Magna T., Wiechert U., Grove T.L., Halliday A.N. (2006) Lithium isotope fractionation in the
1011 southern Cascadia subduction zone. *Earth Planet. Sci. Lett.* **250** (3), 428–443.

1012Magna T., Ionov D. A., Oberli F., Wiechert U. (2008) Links between mantle metasomatism and
1013 lithium isotopes: Evidence from glass-bearing and cryptically metasomatized xenoliths from
1014 Mongolia. *Earth Planet. Sci. Lett.* **276**, 214−222.

1015Marschall H. R., Pogge von Strandmann P. A. E., Seitz H. M., Elliott T., Niu Y. L. (2007) The lithium
1016 isotopic composition of orogenic eclogites and deep subducted slabs. *Earth Planet. Sci. Lett.*
1017 **262**, 563−580.

1018Matthews N. E., Vazquez J. A., Calvert A. (2015) Age of the Lava Creek supereruption and magma
1019 chamber assembly at Yellowstone based on $^{40}Ar/^{39}Ar$ and U–Pb dating of sanidine and zircon
1020 crystals. *Geochem. Geophys. Geosyst*. **16**.

1021Moriguti T., Nakamura E. (1998) Across-arc variation of Li isotopes in lavas and implications for
1022 crust/mantle recycling at subduction zones. *Earth Planet. Sci. Lett.* **163** (1–4), 167–174.

1023Myers M.L., Wallace P.J., Wilson C.J., Morter B.K., Swallow E.J. (2016) Prolonged ascent and
1024 episodic venting of discrete magma batches at the onset of the Huckleberry Ridge
1025 supereruption, Yellowstone. *Earth Planet. Sci. Lett.* **451**, 285-297.

1026Myers M. L., Wallace P. J., Wilson C. J. N., Watkins J. M., Liu Y. (2018) Ascent rates of rhyolitic
1027 magma at the onset of three caldera-forming eruptions. *Am. Mineral.* **103**, 952−965.

1028Myers M. L., Wallace P. J., Wilson C. J. N. (2019) Inferring magma ascent timescales and
1029 reconstructing conduit processes in explosive rhyolitic eruptions using diffusive losses of
1030 hydrogen from melt inclusions. *J. Volcanol. Geotherm. Res.* **369**, 95−112.

1031Neukampf J., Ellis B.S., Magna T., Laurent O., Bachmann, O. (2019) Partitioning and isotopic
1032 fractionation of lithium in mineral phases of hot, dry rhyolites: The case of the Mesa Falls
1033 Tuff, Yellowstone. *Chem. Geol.* **506**, 175–186.

1034Neukampf J., Ellis B.S., Laurent O., Steinmann L. K., Ubide T., Oeser M., Magna T., Weyer S.,
1035 Bachmann O. (2021) Time scales of syn-eruptive volatile loss in silicic magmas quantified by
1036 Li-isotopes. *Geology* **49**, 125−129.

1037Newman S., Epstein S., Stolper E. (1988). Water, carbon dioxide, and hydrogen isotopes in glasses
1038 from the ca. 1340 AD eruption of the Mono Craters, California: Constraints on degassing
1039 phenomena and initial volatile content. *J. Volcanol. Geotherm. Res.* **35**, 75–96.

1040Nielsen R. L., Michael P. J., Sours-Page R. (1998) Chemical and physical indicators of compromised
1041 melt inclusions. *Geochim. Cosmochim. Acta* **62**, 831–839.

1042Parkinson I. J., Hammond S. J., James R. H., Rogers N. W. (2007) High-temperature lithium isotope
1043 fractionation: insights from lithium isotope diffusion in magmatic systems. *Earth Planet. Sci.*
1044 *Lett.* **257**, 609−621.

1045Pearce N. J. G., Westgate J. A., Perkins W. T. (1996) Developments in the analysis of volcanic glass
1046 shards by laser ablation ICP-MS: quantitative and single internal standard-multielement
1047 methods. Quaternary International **34–36**, 213–227.

1048Perkins M. E., Nash B. P. (2002) Explosive silicic volcanism of the Yellowstone hotspot: the ash fall
1049 tuff record. *Geol. Soc. Am. Bull.* **114** (3), 367–381.

1050Perny B., Eberhardt P., Ramseyer K., Mullis J., Pankrath R. (1992) Microdistribution of Al, Li, and
1051 Na in α quartz: Possible causes and correlation with short-lived cathodoluminescence. *Am.*
1052 *Mineral.* **77** (5-6), 534–544.

1053Peterková T., Dolejš D. (2019) Magmatic-hydrothermal transition of Mo-W-mineralized granite-
1054 pegmatite-greisen system recorded by trace elements in quartz: Krupka district, Eastern Krušné
1055 hory/Erzgebirge. *Chem. Geol*. **523**.

1056Qin Z., Lu F., Anderson Jr. A. T. (1992) Diffusive reequilibration of melt and fluid inclusions. *Am.*
1057 *Mineral.* **77**, 565−576.

1058Richter F. M., Davis A. M., DePaolo D. J., Watson E. B. (2003) Isotope fractionation by chemical
1059 diffusion between molten basalt and rhyolite. *Geochim. Cosmochim. Acta* **67**, 3905–3923.

1060Richter F. M., Watson E. B., Mendybaev R., Dauphas N., Georg B., Watkins J., Valley J. (2009)
1061 Isotopic fractionation of the major elements of molten basalt by chemical and thermal
1062 diffusion. *Geochim. Cosmochim. Acta* **73**, 4250–4263.

1063Rivera T. A., Schmitz M. D., Crowley J. L., Storey M. (2014) Rapid magma evolution constrained by
1064 zircon petrochronology and 40Ar/39Ar sanidine ages for the Huckleberry Ridge Tuff,
1065 Yellowstone, USA. *Geology* **42**, 643–646.

1066Rivera T.A., Schmitz M.D., Jicha B.R., Crowley J.L (2016) Zircon petrochronology and $^{40}Ar/^{39}Ar$
1067 sanidine dates for the Mesa Falls Tuff: crystal-scale records of magmatic evolution and the
1068 short lifespan of a large Yellowstone magma chamber. *J. Petrol.* **57**, 1677-1704.

1069Roedder E. (1979) Origin and significance of magmatic inclusions. *Bull. Mineral.* **102**, 487–510.

1070Rose-Koga E., Bouvier A.-S., Gaetani G., Wallace P. J., Allison C. M., Andrys J. A., et al. (2021).
1071 Silicate melt inclusions in the new millennium: a review of recommended practices for
1072 preparation, analysis, and data presentation. *Chem. Geol.* **570**, 120145.

1073Rottier B., Rezeau H., Casanova V., Kouzmanov K., Moritz R., Schlöglova K., Wälle M., Fontboté L.
1074 (2017) Trace element diffusion and incorporation in quartz during heating experiments.
1075 *Contrib. Mineral. Petrol.* **172**, 23.

1076Rowe M. C., Kent A. J. R., Thornber C.R. (2008) Using amphibole phenocrysts to track vapor transfer
1077 during magma crystallization and transport: an example from Mount St. Helens, Washington.
1078 *J. Volcanol. Geotherm. Res.* **178**, 593-607.

1079Sartbaeva A., Wells S. A., Redfern S. A. T., Hinton R. W., Reed S. J. B. (2005) Ionic diffusion in
1080 quartz studied by transport measurements, SIMS and atomistic simulations. *J. Phys. Condens.*
1081 *Matter* **17**, 1099-1112.

1082Schiavi F., Katsura Kobayashi K., Moriguti T., Nakamura E., Pompilio M., Tiepolo M., Vannucci R.,
1083 (2010) Degassing, crystallization and eruption dynamics at Stromboli: trace element and
1084 lithium isotopic evidence from 2003 ashes. *Contrib. Mineral. Petrol* **159**, 541-561.

1085Schiavi F., Kobayashi K., Nakamura E., Tiepolo M., Vannucci R. (2012) Trace element and Pb-B-Li
1086 isotope systematics of olivine-hosted melt inclusions: insights into source metasomatism
1087 beneath Stromboli (southern Italy). *Contrib. Mineral. Petrol.* **163**, 1011–1031.

1088Severs M. J., Azbej T., Thomas J. B., Mandeville C. W., Bodnar R. J. (2007) Experimental
1089 determination of H_2O loss from melt inclusions during laboratory heating: evidence from
1090 Raman spectroscopy. *Chem. Geol.* **237**, 358-371.

1091Singer B. S., Jicha B. R., Condon D. J., Macho A. S., Hoffman K. A., Dierkhising J., Brown M. C.,
1092 Feinberg J. M., Kidane T. (2014) Precise ages of the Reunion event and Huckleberry Ridge
1093 excursion: episodic clustering of geomagnetic instabilities and the dynamics of flow within the
1094 outer core. *Earth Planet. Sci. Lett*. **405**, 25–38.

1095Stalder R., Konzett J. (2012) OH defects in quartz in the system quartz–albite–water and granite–water
1096 between 5 and 25 kbar. *Phys. Chem. Minerals.* **39**, 817–827.

1097Steinmann L. K., Oeser M., Horn I., and Weyer S. (2020) Multi-stage magma evolution in intra-plate
1098 volcanoes: Insights from combined in situ Li and Mg-Fe chemical and isotopic diffusion
1099 profiles in olivine. *Frontiers Earth Sci.* **8**, 201.

1100Swallow E. J., Wilson C. J. N., Charlier B. L. A., Gamble J. A. (2018) Mafic inputs into the rhyolitic
1101 magmatic system of the 2.08 Ma Huckleberry Ridge eruption, Yellowstone. *Am. Mineral.* **103**
1102 (5), 757–775.

1103Teng F. Z., McDonough W. F., Rudnick R. L., Dalpé C., Tomascak P. B., Chappell B. W., Gao S.
1104 (2004) Lithium isotopic composition and concentration of the upper continental crust.
1105 *Geochim. Cosmochim. Acta* **68** (20), 4167–4178.

1106Tollan P. M. E., O'Neill H. S. C., Hermann J. (2018) The role of trace elements in controlling H
1107 incorporation in San Carlos olivine. *Contrib. Mineral. Petrol.* **173**, 89, Doi: 10.1007/s00410-
1108 018-1517-7.

1109Tollan P., Ellis B., Troch J., Neukampf J. (2019) Assessing magmatic volatile equilibria through FTIR
1110 spectroscopy of unexposed melt inclusions and their host quartz: a new technique and
1111 application to the Mesa Falls Tuff, Yellowstone. *Contrib. Mineral. Petrol.* **174** (24).

1112Tomascak P.B., Carlson R.W., Shirey S.B. (1999a) Accurate and precise determination of Li isotopic
1113 compositions by multi-collector sector ICP-MS. *Chem. Geol.* **158**,145−154.

1114Tomascak P. B., Langmuir C. H., le Roux P. J., Shirey S. B. (2008) Lithium isotopes in global mid-
1115 ocean ridge basalts. *Geochim. Cosmochim. Acta* **72** (6), 1626–1637.

1116Tomascak P. B., Magna T. Dohmen R. (2016) Advances in Lithium Isotope Geochemistry. Springer
1117 International Publishing, Cham, Switzerland.

1118Viccaro M., Cannata A., Cannavò F. De Rosa R., Giuffrida M., Nicotra E., Petrelli M., Sacco G. (2021)
1119 Shallow conduit dynamics fuel the unexpected paroxysms of Stromboli volcano during the
1120 summer 2019. *Sci. Rep.* **11**, 266.

1121Vlastélic I., Staudacher T., Bachèlery P., Télouk P., Neuville D., Benbakkar M. (2011) Lithium isotope
1122 fractionation during magma degassing: Constraints from silicic differentiates and natural gas
1123 condensates from Piton de la Fournaise volcano (Réunion Island). *Chem. Geol.* **284** (1-2), 26-
1124 34.

1125Watson E.B. (2017) Diffusive fractionation of volatiles and their isotopes during bubble growth in
1126 magmas. *Contrib. Mineral. Petrol.* **172**.

1127Webster J. D., Holloway J. R., Hervig, R. L. (1989) Partitioning of lithophile trace elements between
1128 H_2O and H_2O + CO_2 fluids and topaz rhyolite melt. *Econ. Geol. Bull. Soc. Econ. Geol*. **84**,
1129 116–134.

1130Wotzlaw, J.-F., Bindeman, I. N., Stern, R. A., D'Abzac, F. X. & Schaltegger, U. (2015). Rapid
1131 heterogeneous assembly of multiple magma reservoirs prior to Yellowstone supereruptions.
1132 *Sci. Rep.* **5**, 14026

1133Zajacz Z., Hanley J.J., Heinrich C.A., Halter W.E., Guillong M. (2009) Diffusive reequilibration of
1134 quartz-hosted silicate melt and fluid inclusions: are all metal concentrations unmodified?
1135 *Geochim. Cosmochim. Acta* **73**, 3013-3027.

1136Zhang Y., Belcher R., Ihinger P. D., Wang L., Xu Z., Newman S. (1997) New calibration of infrared
1137 measurement of dissolved water in rhyolitic glasses. *Geochim. Cosmochim. Acta* **61**, 3089–
1138 3100.

Figure Captions

Figure 1 – Aerial photograph centred on the Yellowstone National Park in NW United States (general location indicated in the inset) showing the geographic extent of Mesa Falls Tuff (dark brown). The sampling location (44°7'8.49"N, 111°26'39.49"W; Ellis et al., 2017) is indicated with a red star. Inferred Henry's Folk caldera (Christiansen, 2001) in light brown and state lines in green. Modified after Neukampf et al. (2021).

Figure 2 – Representative images of double-polished quartz crystals and their melt inclusion populations (**A**) Transmitted light image of a quartz with glassy melt inclusions (MI1 and MI3 = brown MI; MI2 = colourless MI, basal pumice sample). (**B**) Back-Scattered Electron (BSE) image of MI2 with SIMS spots and corresponding δ^7Li values (larger spots correspond to the analysis of δ^{11}B, whose results are not presented here). The uncertainty on the δ^7Li measurements is up to 2‰. (**C**) BSE image of MI1 with gold (Au) coating filling a crack. The arrows indicate SIMS spots and corresponding δ^7Li values. (**D**) Transmitted light image of a quartz with crystallised MIs (flow pumice sample). (**E**) and (**F**) BSE images of MI1 and MI2 from (D), showing that the crystallised fraction mainly consists of tiny (<1 µm) quartz crystals and a thin quartz layer formed at the inner rim of the MI.

Figure 3 – (**A**) Plot of Sm (considered immobile during degassing) vs. Li concentrations in the analysed MIs (colourless, brown or with a bubble; MIs in the figures are displayed with the same symbol) and groundmass glass (gg). Literature data by Neukampf et al. (2019) are plotted for comparison. Crystallised MIs are enriched in Li and glassy MIs have a lower Li concentration than corresponding groundmass glass. Pale yellow (basal pumice) and purple (flow pumice) bands indicate the ranges of Li concentration in the host quartz. (**B**) Plot of Rb

(proxy for contamination from host quartz, as concentrations would strongly decrease whenever the laser spot used for measurement includes host-quartz) vs. Li concentrations of glassy MIs (multiple points per MI), distinguishing measurements occurring in the rim vs. the core of the MIs. Rim and Core pairs are connected by grey tie lines.

Figure 4 – CL images of quartz in the flow pumice (**A**) and basal pumice sample (**B**) (MI = melt inclusion) with measured LA-ICP-MS trace element profiles in light blue (red indicates failed measurement), and diagrams showing concentrations of several elements (Li, Al, P and Ti in ppm) along the corresponding profiles (**C** and **D**). Figure 4A and 4B show one example of representative quartz crystals from each sample. (**E**) Additional Li concentration profile from a quartz from the flow pumice sample with an increase of Li content towards the rim and a decrease towards the MI. (**F**) Additional Li concentration profile from a quartz crystal from the basal pumice sample with an increase of Li content towards the MI. Grey bar shows area with no meaningful data.

Figure 5 – (**A**) Focal plane array FTIR image of a quartz crystal from the flow pumice sample from MFT, colour-coded for IR absorbance. Red line represents an extracted profile shown in (B). Inset shows transmitted light image of the quartz crystal. (**B**) A representative rim-to-rim IR absorption profile in the crystal shown in (A). As the orientation of the crystal is unknown the H_2O concentration is reported as an overtone. (**C**) CO_2 versus H_2O concentrations of glassy MIs from the basal pumice sample compared to literature data (Tollan et al. 2019 for Mesa Falls Tuff and Myers et al. 2016 for Huckleberry Ridge Tuff). Blue lines are volatile saturation isobars calculated at 800 °C, using VolatileCalc (Newman and Lowenstern 2002). (**D**) Lithium

versus H_2O concentrations in glassy MIs from the basal pumice sample of MFT and literature data (Myers et al. 2016, Tollan et al. 2019).

Figure 6 – Plot of Li isotopic composition (as δ^7Li relative to L-SVEC reference material) versus Li concentration of glassy MIs and groundmass glass (gg). Symbols for MIs have an additional green (core), purple (intermediate zone) or yellow (rim) frame representing the position of the MI in the quartz crystal based on CL images. Rim and Core pairs are connected by grey tie lines. Red stars indicate MIs where the Li concentration was not obtained by LA-ICP-MS but recalculated from Li concentration determined by SIMS.

Figure 7 – Plot of Li versus Al concentrations in quartz from the MFT samples. The black thick line represents the isoatomic Li:Al 1:1 line (ideal substitution of $Si^{4+} \leftrightarrow Al^{3+} + Li^{+}$), whereas the two coloured lines consider that Al incorporation is charge balanced by both Li^{+} + H^{+}, with two different corresponding H_2O concentrations.

Figure 8 – Plot of Li isotopic composition (as δ^7Li relative to L-SVEC reference material) versus Li concentration showing the results of models of Li elemental and isotopic evolution during the two inferred degassing stages (stage 1 in the magma reservoir, stages 2/3 in the conduit immediately before eruption) and the data from MIs and groundmass glass in MFT samples. Data is displayed in grey when not relevant for the degassing stage considered in the modelling scenario. Tick marks indicate the fraction of degassed Li (in %) based on the model. (**A**) An open-system degassing model driven by kinetic fractionation, considering two different $\alpha_{vapour-melt}$ values (0.965 and 0.978) with four different values of $D_{vapour-melt}$ (1, 1.5, 2, 3). (**B**) A model of open-system equilibrium degassing model considering four different $D_{vapour-melt}$ values. (**C**) A model of open-system equilibrium degassing scenarios using different $\alpha_{vapour-}$

1204 $_{melt}$ with two different starting points (δ^7Li = 12.0‰ and Li = 51.4 ppm; δ^7Li = 9.9‰ and Li =
1205 59.9 ppm, respectively). (**D**) A model of closed-system degassing (Rayleigh fractionation)
1206 using three different $\alpha_{vapour-melt}$ values (1.005, 1.010, 1.015).

1207 **Figure 9** – Cartoon portraying a simplified model (not to scale) of the processes recorded in
1208 two investigated samples from the Mesa Falls Tuff. (**A**) Stage 1 represents Li isotopic
1209 composition of the melt in the magma reservoir prior to eruption with (1) equilibrium
1210 degassing in the magma reservoir leading to a progressively lighter Li isotopic composition of
1211 the melt. (**B)** Stage 2 shows open-system disequilibrium degassing in the conduit leading to
1212 the modification of Li isotopic composition and Li concentration of MIs, quartz crystals and
1213 groundmass glass in the basal pumice sample (2). (**C)** Stage 3 with prolonged open-system
1214 disequilibrium degassing and the influence on the flow pumice sample (6). (**D**) A detailed
1215 scheme of degassing of volatile phases (e.g., Li and H) with ^{6}Li moving faster into the volatile
1216 phase (4), ultimately leading to kinetic fractionation and the Li isotopic composition of glass
1217 becoming heavier. Small-scale diffusional exchange of H^+ and Li^+ causes H^+ diffusing out of
1218 the host quartz into the melt and Li^+ diffusing inwards (5); and Li^+ diffusing into an MI to
1219 charge balance H^+ loss (6). Below a theoretical profile of Li and H concentration of the host
1220 quartz in (D). **(E)** Continuing degassing influenced the Li isotopic composition of the
1221 groundmass glass (7) resulted in prolonged $H^+ \leftrightarrow Li^+$ diffusional exchange between quartz and
1222 melt (8): $H^+ \leftrightarrow Li^+$ and (9) shows. H^+/OH^- diffusing out of MI lead to crystallisation of the MI
1223 and Li^+ diffusing therein for charge balance (9). Below a theoretical profile of Li and H
1224 concentration in the host quartz shown in (E).

1225

Table 1. Trace element concentrations in glassy and crystallised MIs and groundmass glass from both samples.

	glassy MI (basal pumice)		**crystallised MI (flow pumice)**		**groundmass glass (basal pumice)**		**groundmass glass (flow pumice)**	
	concentration (ppm)	avg. (ppm)	concentration (ppm)	avg. (ppm)	concentration (ppm)	avg. (ppm)	concentration (ppm)	avg. (ppm)
Zr	85–185	133	73–204	143	128–175	156	123–176	157
Ba	4–139	58	1–151	36	43–302	138	85–355	132
Rb	157–322	236	115–370	232	223–293	243	216–265	237
Sm	6–14	9	4–13	9	9–15	11	8–13	11
Li	10–61	34	9–190	76	32–46	41	32–51	41

Figure 1

Click here to access/download;Figure

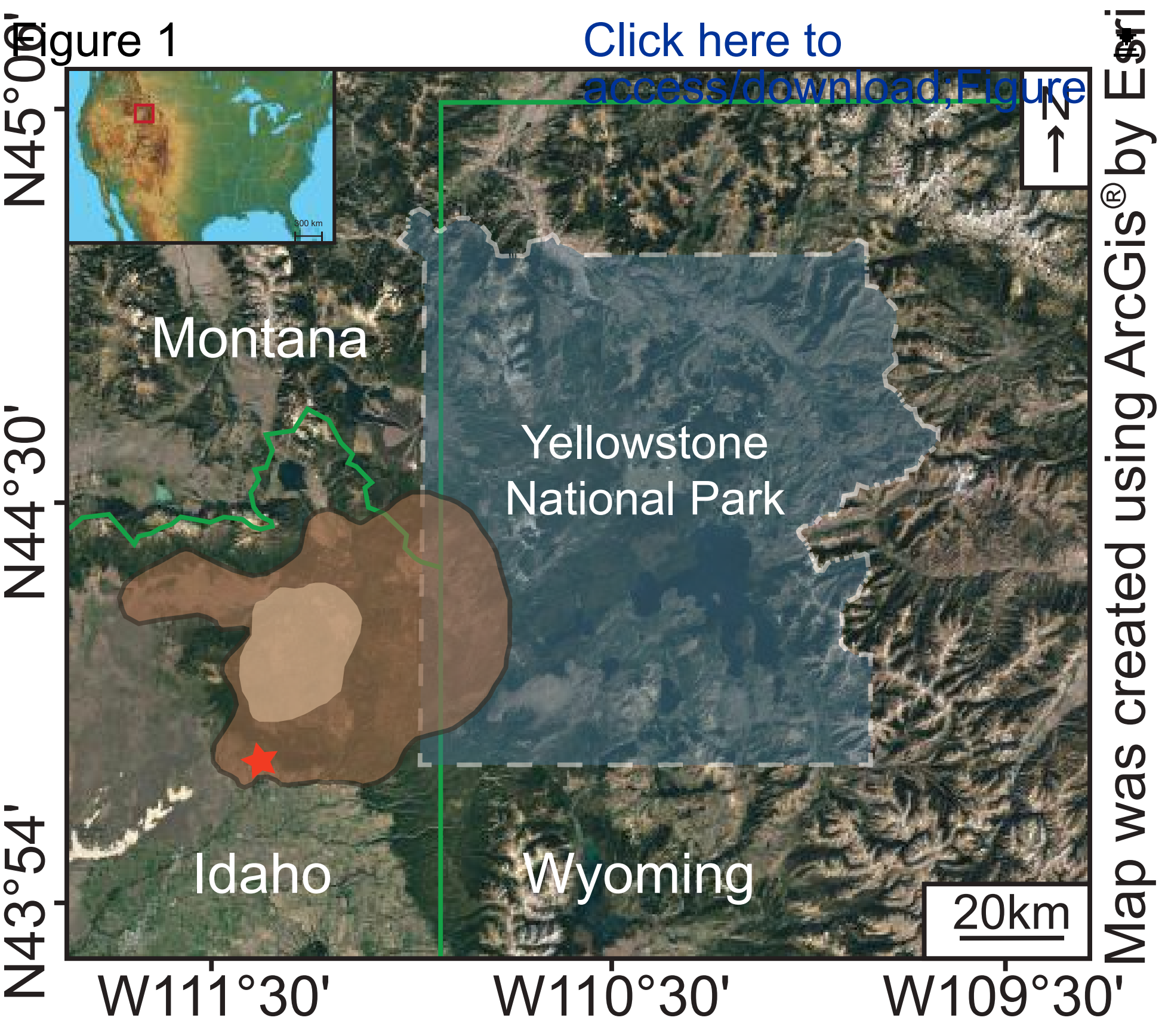

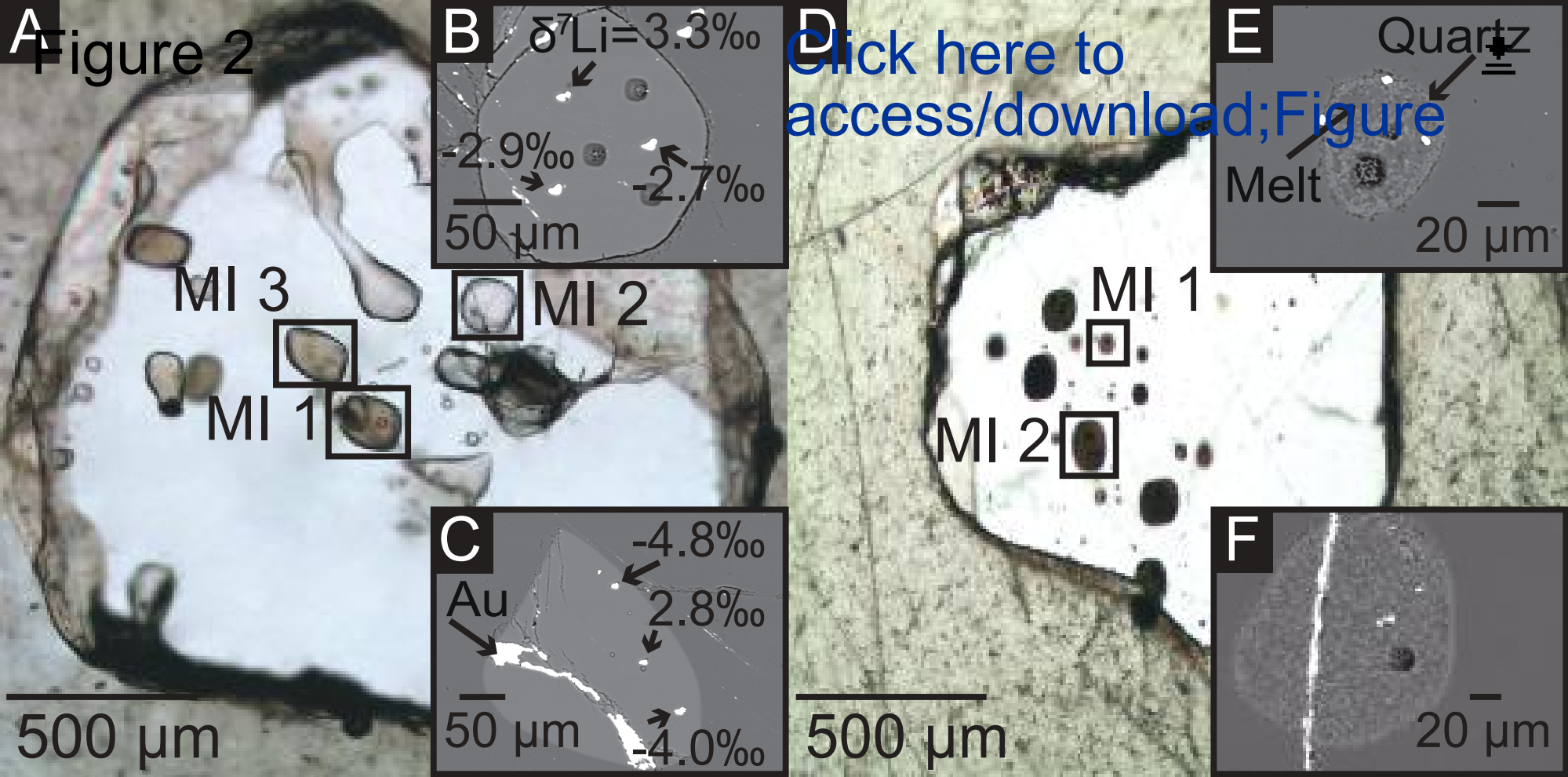
Figure 2
A
MI 3
MI 1
500 µm
B
δ7Li=3.3‰
-2.9‰
-2.7‰
50 µm
MI 2
C
-4.8‰
Au
2.8‰
50 µm
-4.0‰
D
Click here to access/download;Figure
MI 1
MI 2
500 µm
E
Quartz
Melt
20 µm
F
20 µm

Figure 3

Click here to access/download;Figure;Figure 3-

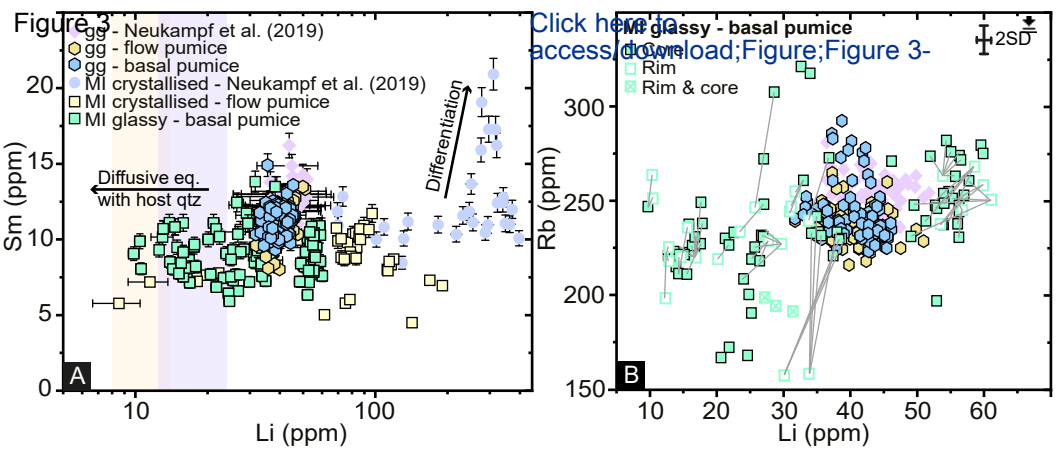

Figure 4

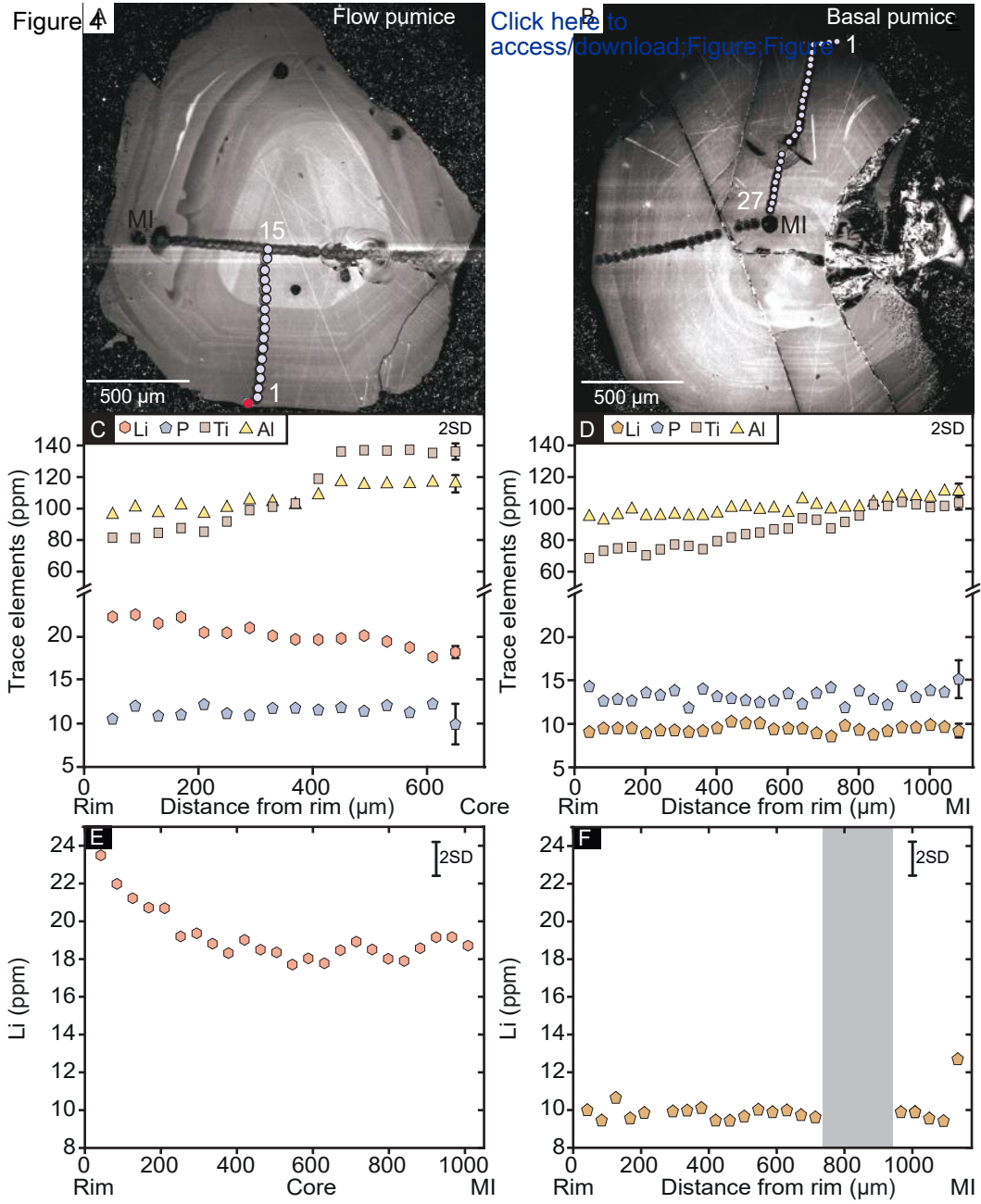

Figure 5

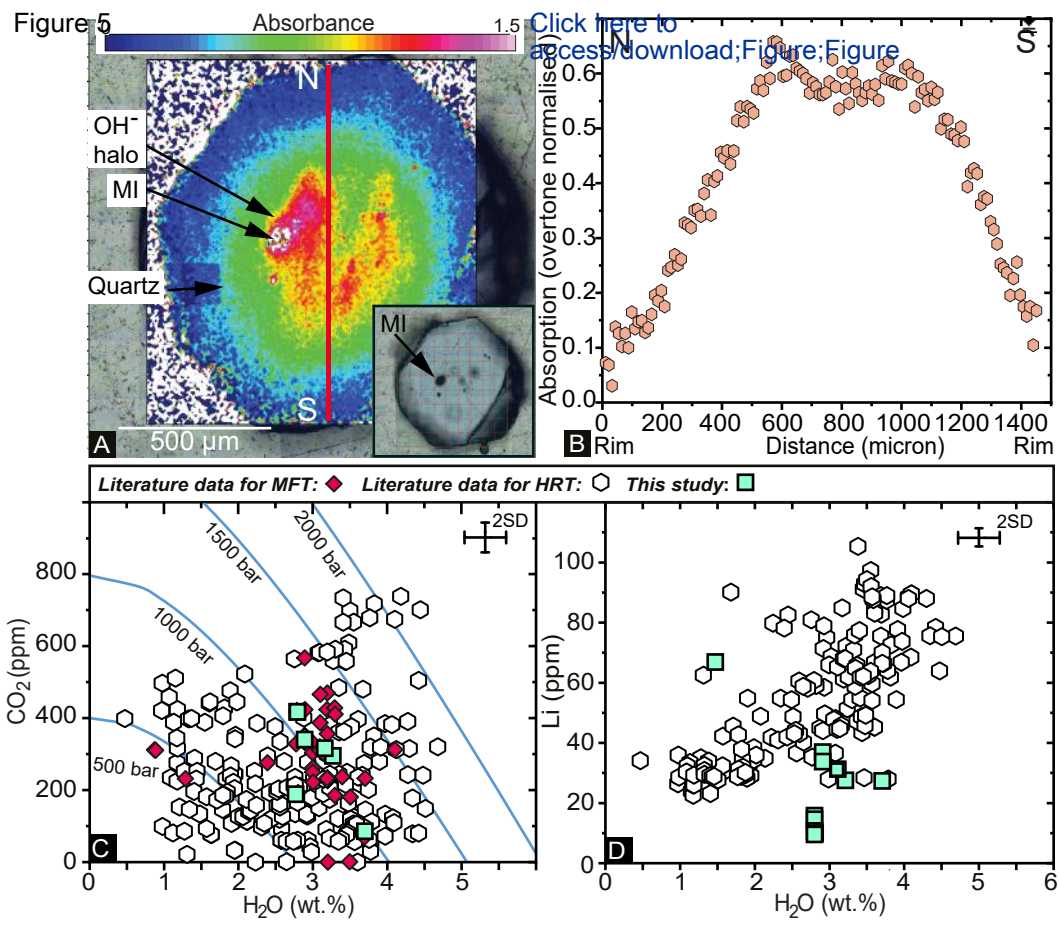
Absorbance
1.5
Click here to access/download;Figure;Figure
N
S
OH⁻ halo
MI
Quartz
MI
A
500 µm
B
Absorption (overtone normalised)
Distance (micron)
Rim
Rim
Literature data for MFT:
Literature data for HRT:
This study:
2SD
1500 bar
2000 bar
1000 bar
500 bar
CO2 (ppm)
H2O (wt.%)
C
Li (ppm)
H2O (wt.%)
D

Figure 6

Click here to access/download;Figur

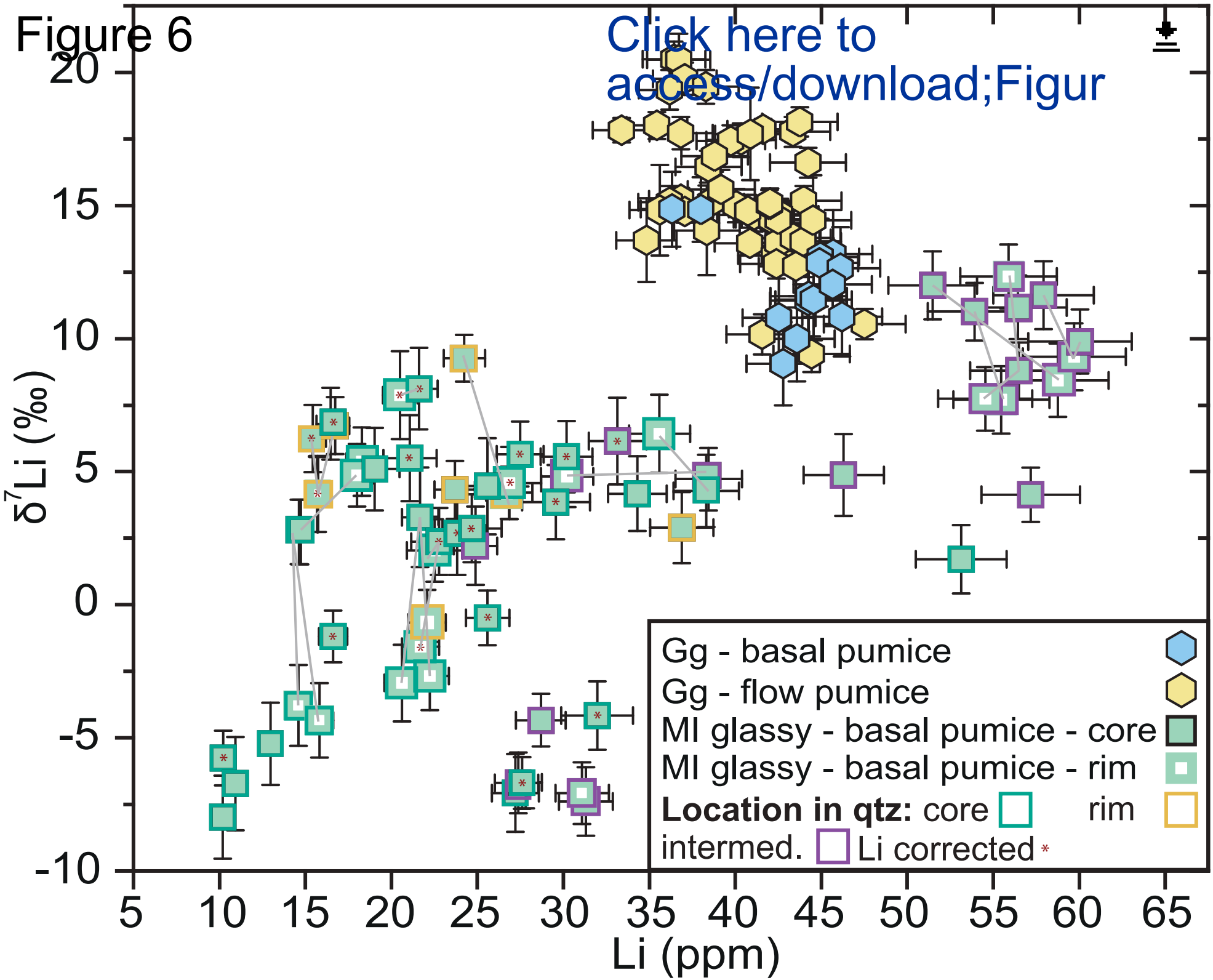

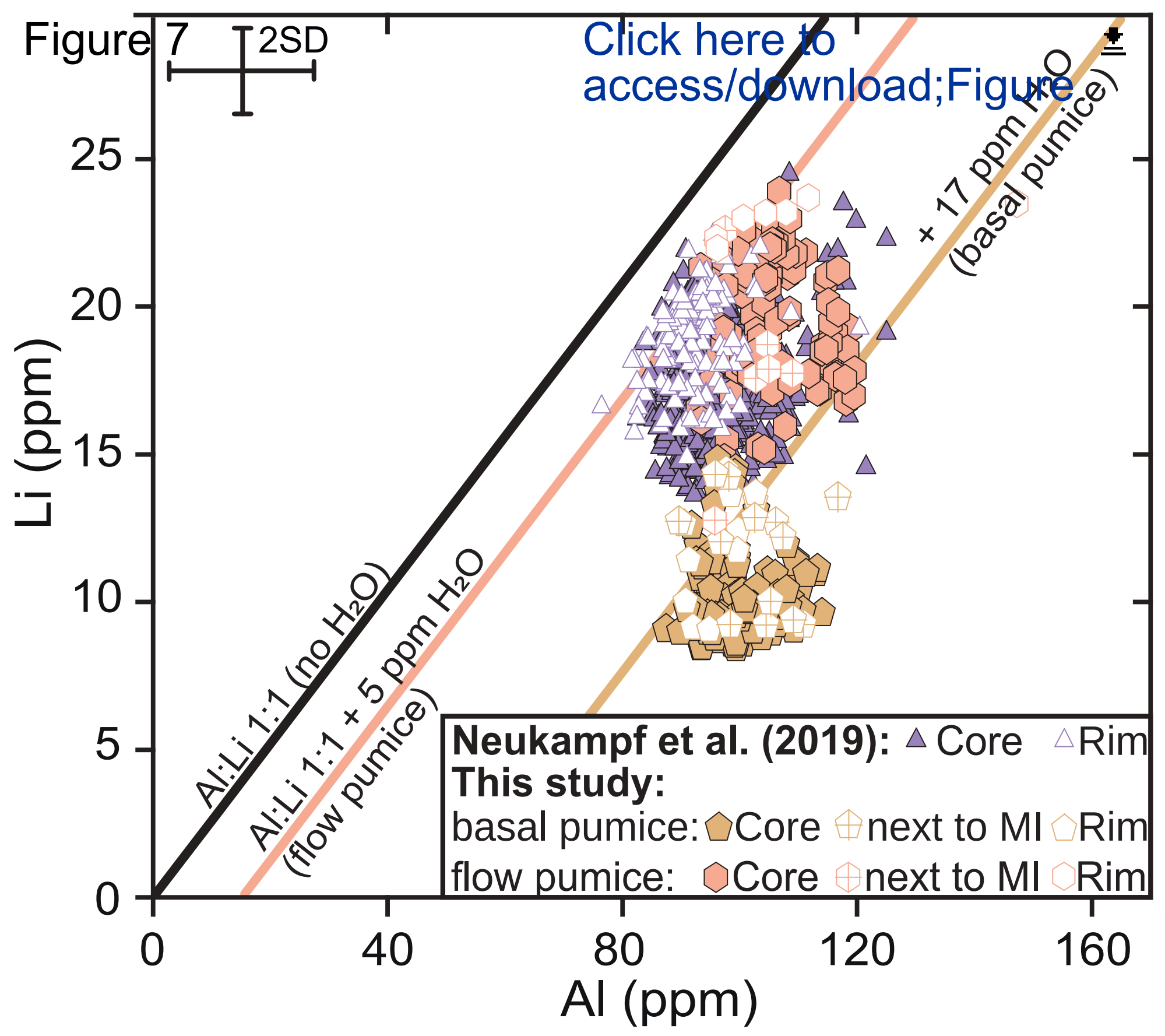
Figure 7
2SD
Click here to access/download;Figure
Li (ppm)
Al (ppm)
0
5
10
15
20
25
0
40
80
120
160
Al:Li 1:1 (no H2O)
Al:Li 1:1 + 5 ppm H2O (flow pumice)
+ 17 ppm H2O (basal pumice)
Neukampf et al. (2019): Core Rim
This study:
basal pumice: Core next to MI Rim
flow pumice: Core next to MI Rim

Figure 8

Click here to access/download;Figure;Figure 8new.pdf

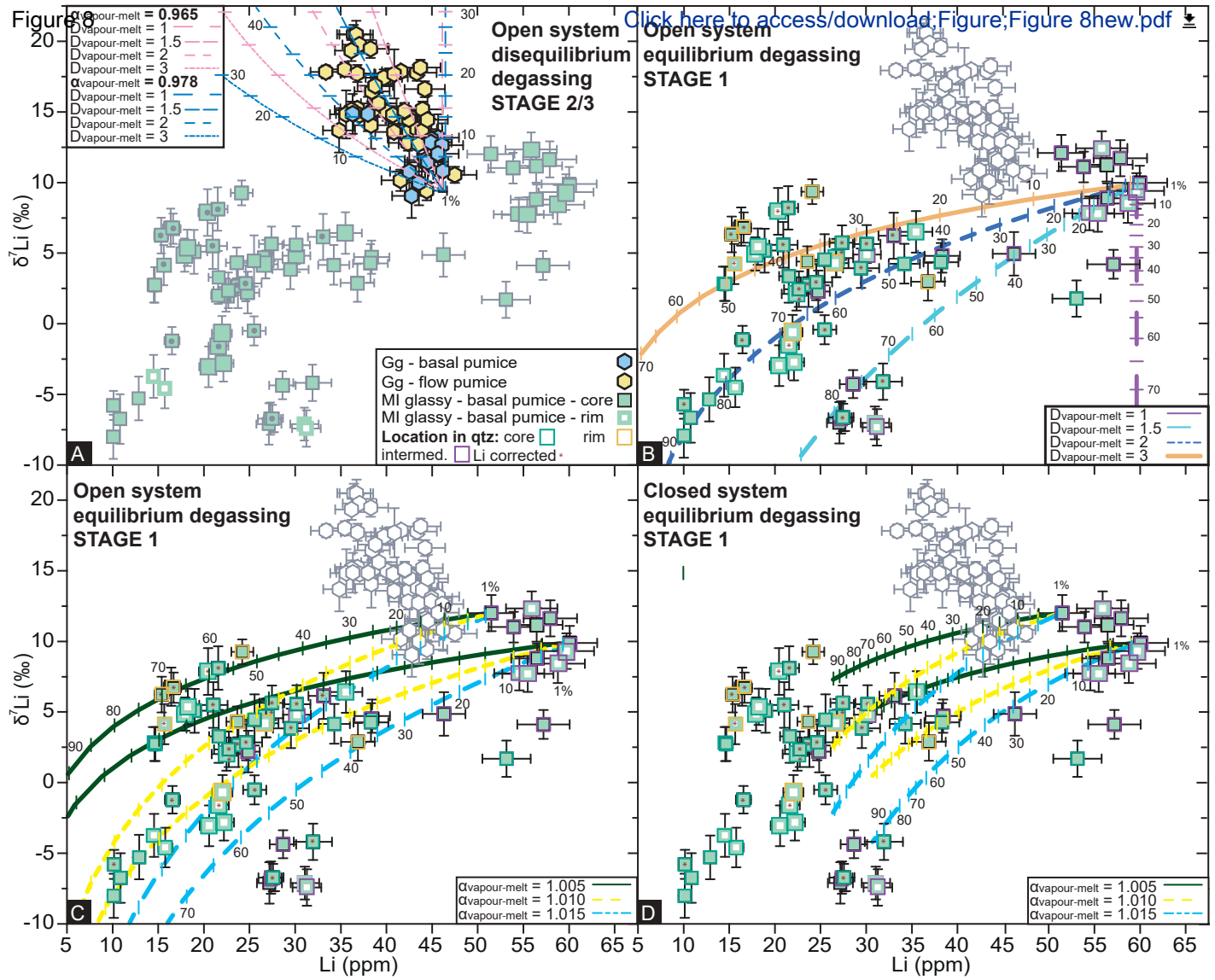

Figure 9

Time

Click here to access/download;Figure;Figure 9new.pdf